Stem Cell Reports
Article
ISSCR
OPEN ACCESS

Neuroinflammation and EIF2 Signaling Persist despite Antiretroviral Treatment in an hiPSC Tri-culture Model of HIV Infection

Sean K. Ryan,[1,2] Michael V. Gonzalez,[6] James P. Garifallou,[6] Frederick C. Bennett,[3] Kimberly S. Williams,[5] Nathaniel P. Sotuyo,[2] Eugene Mironets,[1] Kieona Cook,[2] Hakon Hakonarson,[6,7] Stewart A. Anderson,[2,3,*] and Kelly L. Jordan-Sciutto[1,4,*]

[1]Department of Pathology, Perelman School of Medicine, University of Pennsylvania, Philadelphia, PA 19104, USA
[2]Department of Psychiatry, The Children's Hospital of Philadelphia, Philadelphia, PA 19104, USA
[3]Department of Psychiatry, Perelman School of Medicine, University of Pennsylvania, Philadelphia, PA 19104, USA
[4]Department of Basic and Translational Sciences, School of Dental Medicine, University of Pennsylvania, Philadelphia, PA 19104, USA
[5]Environmental and Health Sciences Program, Spelman College, Atlanta, GA 30314, USA
[6]Center for Applied Genomics, Children's Hospital of Philadelphia, The Perelman School of Medicine, University of Pennsylvania, Philadelphia, PA 19104, USA
[7]Division of Human Genetics, Department of Pediatrics, The Perelman School of Medicine, University of Pennsylvania, Philadelphia, PA 19104, USA
*Correspondence: sande@pennmedicine.upenn.edu (S.A.A.), jordank@upenn.edu (K.L.J.-S.)
https://doi.org/10.1016/j.stemcr.2020.02.010

SUMMARY

HIV-associated neurocognitive disorders (HAND) affect over half of HIV-infected individuals, despite antiretroviral therapy (ART). Therapeutically targetable mechanisms underlying HAND remain elusive, partly due to a lack of a representative model. We developed a human-induced pluripotent stem cell (hiPSC)-based model, independently differentiating hiPSCs into neurons, astrocytes, and microglia, and systematically combining to generate a tri-culture with or without HIV infection and ART. Single-cell RNA sequencing analysis on tri-cultures with HIV-infected microglia revealed inflammatory signatures in the microglia and EIF2 signaling in all three cell types. Treatment with the antiretroviral compound efavirenz (EFZ) mostly resolved these signatures. However, EFZ increased RhoGDI and CD40 signaling in the HIV-infected microglia. This activation was associated with a persistent increase in transforming growth factor α production by microglia. This work establishes a tri-culture that recapitulates key features of HIV infection in the CNS and provides a new model to examine the effects of infection, its treatment, and other co-morbid conditions.

INTRODUCTION

HIV-associated neurocognitive disorders (HAND) are a chronic, progressing spectrum of diseases that lead to a range of neurologic disorders, including HIV-associated dementia. The major pathologic manifestation that persists in HAND patients with antiretroviral treatment (ART) is synaptodendritic damage and the accumulation of microglia, the resident immune cell of the central nervous system (CNS); however, the mechanisms underlying synaptic damage remain elusive. Synapse loss is associated with infiltration of macrophages from outside of the CNS and activation of microglia. Both HIV-infected macrophage populations can release cytokines, viral proteins, and excitotoxins, which can lead to synaptic damage (Saylor et al., 2016) and are potential reservoirs for the virus (Castellano et al., 2017). Although patients on ART experience milder forms of HAND, they still experience chronic inflammation (Kolson, 2017). Infected microglia and uninfected, but active microglia may be working in tandem to slowly release proinflammatory cytokines and reactive oxygen species that, over time, can lead to synaptodendritic damage (Sui et al., 2007; Turchan–Cholewo et al., 2009). Additional aspects of inflammatory responses have been implicated in HAND, including the unfolded protein response (UPR) and its resultant activation of EIF2 (Akay et al., 2012; Jiang et al., 2017; Lindl et al., 2007).

Although the major pathological manifestation of HAND is synaptodendritic damage, the response during initial exposure to HIV and ART is unknown largely because current models for HIV-mediated neuroinflammation are limited by species differences and human tropism of the virus. For instance, the HIV-1 Tat transgenic mouse model exhibits neuroinflammation and behavioral deficits, but it only expresses a single viral protein from astrocytes (Kim et al., 2003). In addition, while isolated microglia from human patients can provide important insights, this is only a snapshot of the end stage of the disease. Therefore, the development of an *in vitro* human system allowing the interaction of the main cell types involved in HAND is needed to further understand the neuropathogenesis and develop novel therapeutics.

We have developed a human-induced pluripotent stem cell (hiPSC)-based model. Whereby, we separately differentiate hiPSCs into forebrain-like excitatory neurons, astrocytes, and microglia, and then combine them to create a tri-culture, with or without HIV infection of the microglia and with or without ART. Our protocol rapidly produces microglia-like cells (iMg) that express multiple classical

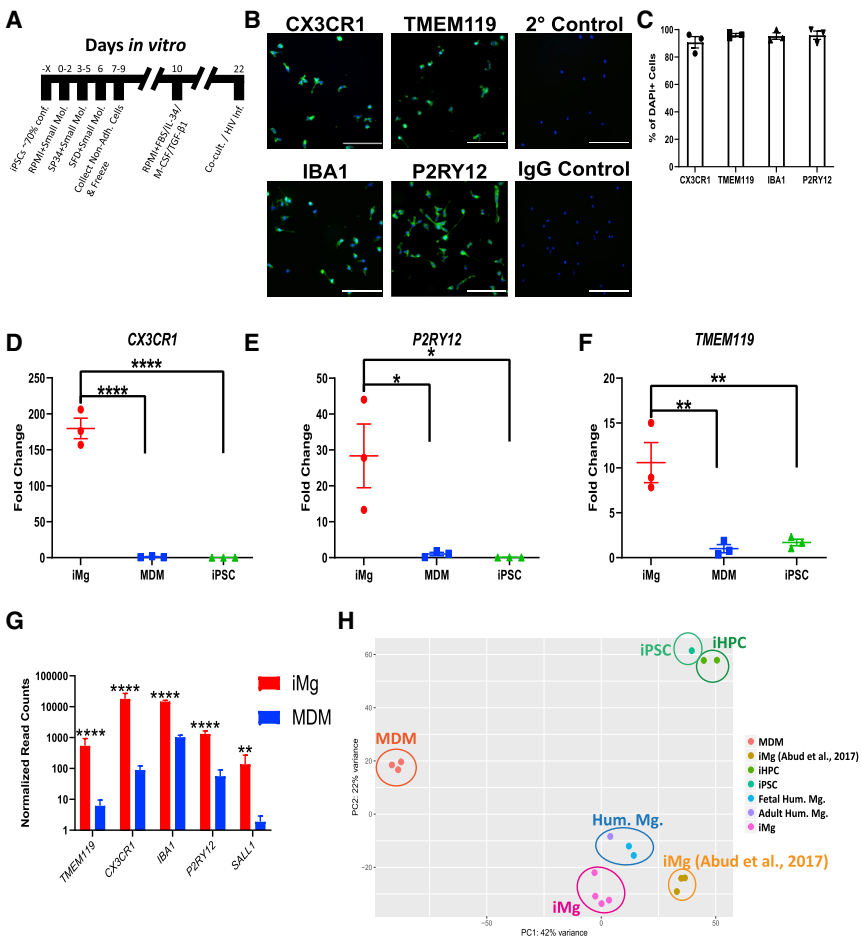

Figure 1. Generation and Characterization of iMg

(A) Timeline for iMg differentiation.

(B) Immunostaining for microglia specific markers: CX3CR1, TMEM119, IBA1, and P2RY12, secondary and IgG controls. All cultures were stained for DAPI. Scale bar represents 50 μm.

(C) Percentage of DAPI(+) cells that are double-positive for microglia marker. n = 3 cell lines, error bars represent SEM.

(D–F) qRT-PCR validation for expression of *CX3CR1* (D), *P2RY12* (E), and *TMEM119* (F) in iMg. Probes normalized to *GAPDH* expression. n = 3 cell lines, one-way ANOVA, Dunnett's post hoc analysis, *p < 0.05, **p < 0.01, ****p < 0.0001; error bars represent SEM.

(G) Bulk RNA-seq normalized read counts of specific microglia markers from iMg and MDMs. n = 4 iMg lines, n = 3 MDMs. Benjamini-Hochberg, false discovery rate (FDR) = 0.01, **p < 0.01, ****p < 0.0001; error bars represent SEM.

(H) Principal-component analysis (PCA) for monocyte-derived macrophages, iMicroglia, and (Abud et al., 2017) iMg, iPSC, iHPC, and primary human microglia. Each dot represents a bulk RNA-seq sample. MDM, monocyte-derived macrophage; iHPC, induced hematopoietic progenitor cells. iPSC, iHPC, Hum. Mg., and iMg samples were all retrieved from Abud et al. (2017).

markers in mono-culture, productively infect with HIV, and respond to ART. In addition, we have developed a differentiation protocol for functional astrocyte-like cells (iAst) that express hallmark proteins. Utilizing this system, we investigated the effects of HIV infection (Inf), infection with the antiretroviral efavirenz (EFZ) (Inf + EFZ), and EFZ treatment alone (Uninf + EFZ), compared to uninfected tri-cultures (Uninf) and to each other. Interestingly, acute HIV infection reduced synaptophagy by both infected iMg and uninfected iMg in the cultures. Inf also caused gene expression changes consistent with activated inflammatory cytokine signaling in iMg and activation of EIF2 signaling in iMg, iAst, and iPSC-derived neurons (iNrn). Although Inf + EFZ reduced many inflammatory markers, EIF2 signaling activation persisted in the iNrn, and RhoGDI and CD40 signaling persisted in the iMg. In addition, EFZ treatment alone invoked its own discrete inflammatory response, reaffirming the toxic effects of EFZ (Ciccarelli et al., 2011) and revealing pathways that may contribute to the toxicity. Our system, which recapitulates key findings in patient studies, provides a platform to mechanistically understand responses to HIV seen in human studies and further reveal the complex roles of the individual cell types during infection ± ART, how ART alone can elicit an inflammatory response, and the prominent role microglia play in the early inflammation response to HIV infection in the brain.

RESULTS

iMicroglia Exhibit Similar Gene and Protein Expression as Other iPSC-Derived Microglia

To develop a tractable system for studying HAND *in vitro*, we adapted two previously published protocols to generate iMg from four separate iPSC lines (Figure 1A). First, iPSCs are differentiated into CD41+ CD235+ common myeloid progenitors (CMPs) through a 9-day process (Paluru et al., 2014). Next, using a modified 11-day protocol (Abud et al., 2017) CMPs are differentiated into a highly pure population of ramified iMg that express CX3CR1, IBA1, TMEM119, and P2RY12 (Figures 1B, 1C, and S1A). Based

on the Abud protocol, we used the small molecules interleukin-34 (IL-34) and colony-stimulating factor 1 (CSF-1), as these are the ligands for CSF1R and are necessary for microglia development *in vivo* (Easley-Neal et al., 2019), and transforming growth factor β1 (TGF-β1), as it helps induce an *in vivo* pattern of gene expression (Gosselin et al., 2017). Fetal bovine serum was implemented to increase viability. iMg exhibited a 179-, 28-, and 11-fold increase in *CX3CR1* ($p < 0.0001$), *P2RY12* ($p < 0.05$), and *TMEM119* ($p < 0.01$), respectively, over monocyte-derived macrophages (MDMs) by qRT-PCR (Figures 1D–1F). Microglial identity was further confirmed by RNA sequencing (RNA-seq) (Figures 1G and S1B). Importantly, iMg also express CCR5 (Figure S1C), one of the co-receptors necessary for HIV infection (Deng et al., 1996). iMg also lacked expression of myeloid progenitor markers (Figure S1F). Finally, we compared our iMg with human MDMs as well as datasets from primary human adult and fetal microglia, iPSCs, induced hematopoietic progenitor cells, and iMicroglia from Abud and colleagues (Abud et al., 2017). Principal-component analysis revealed closer clustering of our iMg (pink) to primary human microglia (blue) than previously published iPSC-derived microglia (light orange) (Figure 1H).

iMg Are Productively Infected with HIV and Respond to Multiple Antiretrovirals

To establish the effect of HIV infection and ART on microglia, we infected iMg mono-culture with 50 ng/mL of the CSF-derived, R5-tropic JAGO strain of HIV (Chen et al., 2002). After a 15-day infection, a time point based on previous studies of MDMs (O'Donnell et al., 2006), 94.5% ± 5.5% of the iMg were positive for the HIV capsid protein P24 and exhibited vast multinucleation (Figures 2A and 2B). Most (89.1% ± 3.8%) P24(+) iMg were multinucleated (Figure 2C), while no P24(−) iMg were multinucleated (Figure 2D), showing that multinucleation is exclusively associated with infection. Reverse transcriptase activity showed peak viral production occurred near day 15 (Figure 2E).

We initially infected iMg from iPSCs of four individuals. Remarkably, the iMg of one individual showed limited infection (Figure S1E). Subsequent genotyping revealed heterozygosity for the CCR5Δ32 mutation, known to reduce infectivity by HIV (Liu et al., 1996) (Figure S1D). This line was thus excluded from subsequent studies, but this example demonstrates the validity of our system to model known regulators of human infection.

To determine if ART can suppress infection in the iMg, we examined the effects of the antiretroviral drug EFZ, a non-nucleoside reverse transcriptase inhibitor (De Clercq, 2004). EFZ remains a first-line drug in many parts of the world (Taramasso et al., 2018). Because EFZ blocks HIV reverse transcription, it had an advantage in allowing the study of non-productively infected, HIV-exposed cells alongside productively infected cells, a scenario thought to occur in brains of ART-treated HIV+ people. At day 15, EFZ reduced the infection rate by two-thirds to 29.2% ± 6.3% (Figures 2A and 2B). Of those iMg infected in the EFZ condition, rates of multinucleation were over 90% and similar to the Inf condition (Figure 2C), and 100% of P24(−) iMg in the Inf+ EFZ culture were single nucleated (Figure 2D). Reverse transcriptase activity was severely reduced with EFZ treatment (Figure 2E). The combined impaired reverse transcriptase and reduced percentage of P24(+) cells shows that EFZ effectively suppressed new infection, allowing us to study both infected and uninfected iMg in the same culture.

Infected iMg Produced Proinflammatory Cytokines at Peak Infection, Which Is Tempered by EFZ Treatment

HIV infection in the CNS leads to changes in cytokine profiles (Ginsberg et al., 2018). Therefore, we quantified the changes in production of relevant cytokines in iMg over the course of infection ± EFZ. Infection led to increased production of several proinflammatory cytokines, specifically IL-1b ($p < 0.01$), IL-1a ($p < 0.05$), transforming growth factor α (TNF-α) ($p < 0.05$), and most prominently, IL-8 ($p < 0.01$) (Figures 2F–2I). However, the two other cytokines tested: IL-6 and IL-10, did not change across any condition (Figures S2A and S2B). It was expected that the anti-inflammatory IL-10 would not increase, but surprising that IL-6 did not increase (Shah et al., 2011).

Infected iMg cultures exposed to EFZ had less production of IL-1b, IL-8, TNF-α, and IL-1a (Figures 2F–2I), suggesting a reduced inflammatory reaction, which recapitulates what is seen in ART-treated patients. Uninf, Uninf + EFZ, and the DMSO vehicle control did not elucidate a cytokine reaction across the six cytokines tested (Figures S2C–S2G).

Infected iMg Have Impaired Cell-Cycle Regulation and DNA Repair and Increased Expression of Inflammatory Genes

To investigative overall gene expression changes during infection, we performed bulk RNA-seq on three iMg lines ± HIV infection, which revealed significant changes in cell-cycle regulation and DNA repair (Figure S3A), consistent with our observation that HIV infection of iMg results in multinucleation. Although no inflammatory pathways were identified by Ingenuity Pathway Analysis, many inflammatory genes involved in the complement system, nuclear factor κB (NF-κB) signaling, and TNF-α signaling were significantly upregulated, as well as *IL1b*, *CCL8*, and *FOS* (Figure S3C).

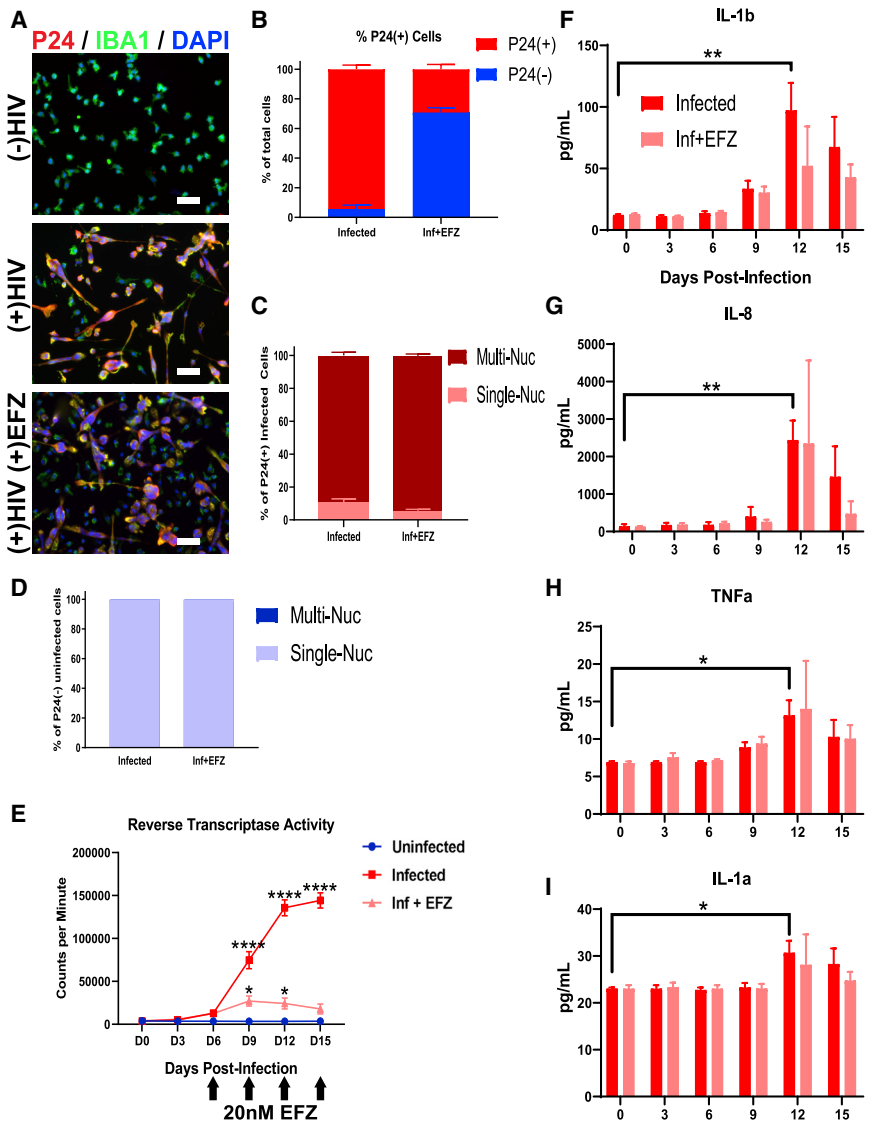

Figure 2. HIV-Infected iMicroglia Produce an Inflammatory Response, and Respond to EFZ

(A) Immunostaining showing reduced percentage of P24+ (red) IBA1+ (green) iMg in HIV-infected mono-cultures + EFZ treatment compared with infected cultures with no EFZ treatment. Scale bar represents 50 μm.

(B) Percentage of P24+ cells in mono-culture iMg at D15 for infected and Inf + EFZ conditions. n = 4 infections from 3 cell lines, error bars represent SEM.

(C) Percent of P24+ single nucleated and multinucleated iMg in mono-culture for infected and Inf + EFZ conditions. n = 4 infections from 3 cell lines.

(D) Percent of P24(−) single nucleated and multinucleated iMg in mono-culture for Inf and Inf + EFZ conditions. n = 4 infections from 3 cell lines.

(E) Reverse transcriptase activity of Uninf, Inf, and Inf + EFZ (20 nM) iMg show productive infection and response to EFZ. n = 3 independent infections of WT6, one-way ANOVA, Dunnett's post hoc analysis; *p < 0.05, ****p < 0.0001; error bars represent SEM.

(F–I) Cytokine analysis of infected iMg mono-culture displays increase in IL-1b (F), IL-8 (G), TNF-α (H), and IL-1a (I) production in the infected iMg. n = 3 independent infections of WT6, one-way ANOVA, Dunnett's post hoc analysis; *p < 0.05, **p < 0.01; error bars represent SEM.

Collectively, these data show that the iMg exhibit an inflammatory response similar to that seen *in vivo* with increased production of IL-8, IL-1b, IL-1a, and TNF-α. This inflammatory response is strongly attenuated with EFZ. RNA-seq analysis revealed changes in cell cycle and inflammation between uninfected and infected iMg as expected.

Generation of iPSC-Derived Tri-cultures of iNeurons, iAstrocytes, and iMicroglia

iNrn were generated by an established protocol that generates a homogeneous population of glutamatergic, forebrain-like excitatory neurons (Zhang et al., 2013). iPSC-derived astrocytes (iAst) were generated by brief exposure of iPSCs to the NGN2 transcription factor used to drive iNrn differentiation, and that *in vivo* is expressed by cortical progenitors before their conversion from neurogenesis to gliogenesis. We noticed that, after 2 days of NGN2 production, cells express the neural progenitor markers Nestin and NCAM and the astrocyte marker SOX9 (Kang et al., 2012) (Figure S4A). Because the NGN2 protocol produces a homogeneous population of neurons, we posited that shifting the differentiation at the neural progenitor stage would yield a relatively homogeneous population of iAst. We thus shifted the differentiation to astrocytes by removing the NGN2-inducing agent doxycycline at day 2, while promoting astrocytic differentiation and proliferation with fibroblast growth factor 2 (FGF-2), epidermal growth factor (EGF), and fetal bovine serum (FBS) (Michler-Stuke et al., 1984). After 70 days the iAst were switched

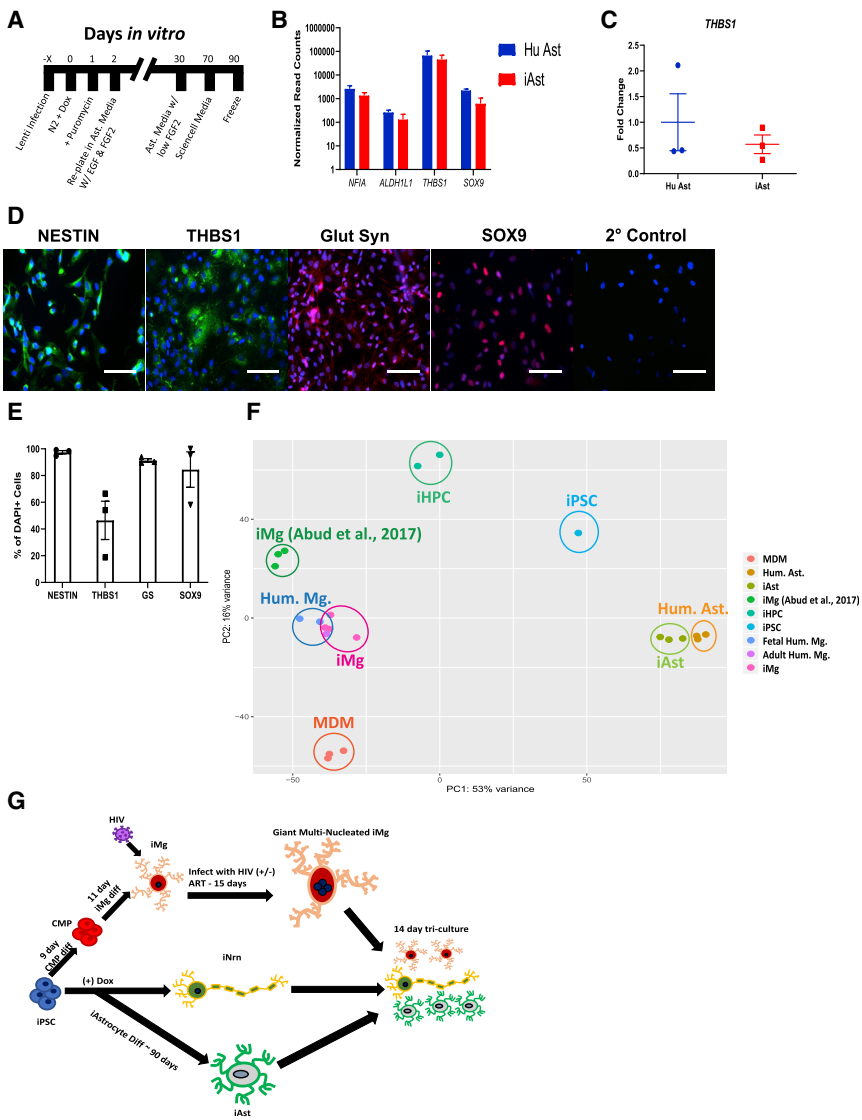

Figure 3. Generation and Characterization of iAst and Formation of Tri-cultures

(A) Timeline for iAstrocyte differentiation.

(B) Bulk RNA-seq normalized read counts of select astrocyte specific genes from primary human astrocytes and iAst. n = 3 cell lines, Benjamini-Hochberg, FDR = 0.01, error bars represent SEM.

(C) qRT-PCR validation for expression of *THBS1* in Hu Ast and iAst. Probe normalized to *GAPDH* expression. n = 3 cell lines, two-tailed t test, error bars represent SEM.

(D) Immunostaining for the astrocyte-specific markers: Nestin, thrombospondin-1, glutamine synthetase, SOX9, and secondary control. Scale bar represents 50 μm.

(E) Percentage of DAPI(+) cells that are double-positive for astrocyte marker. n = 3 cell lines, error bars represent SEM.

(F) PCA for monocyte-derived macrophages, iMicroglia, primary human astrocytes, and iAstrocytes, and (Abud et al., 2017) iMg, iPSC, iHPC, and primary human microglia. Each dot represents a bulk RNA-seq sample. MDM, monocyte-derived macrophage; Hum. Ast., primary fetal human astrocytes; iHPC, induced hematopoietic progenitor cells. iPSC, iHPC, Hum. Mg., iMg samples were all retrieved from Abud et al. (2017).

(G) Flowchart for differentiations into iMg, iAst, and iNrn and combination into tri-culture ± HIV infection and ART.

to Sciencell Astrocyte Media (Figure 3A). After 90 days, RNA-seq revealed similar overall gene expression between iAst and fetal human astrocytes (Hu Ast), including several key astrocyte genes (Figures 3B and 3F). qRT-PCR validation of *THBS1* confirmed similar expression Hu Ast and iAst (Figure 3C). We confirmed several of these genes at the protein level, including Nestin, glutamine synthetase, THBS1, an important protein in early synaptogenesis (Christopherson et al., 2005), and SOX9, revealing a relatively homogeneous population (Figures 3D and 3E). The iAst exhibited modest glutamate uptake and propagated Ca^{2+} waves in a gap junction-dependent manner, demonstrated by halted Ca^{2+} propagation with 100 μM carbenoxolone, a gap junction blocker (Figures S4F–S4I and Video S1). While in mono-culture, the iAst did not detectably express GFAP, GLT-1, or GLAST (Figures S4B–S4D), in tri-culture, single-cell RNA-seq (scRNA-seq) showed expression of *GLT-1* in iAst (Figure S4E). As neuronal activity regulates GLT-1 in astrocytes (Swanson et al., 1997), iAst have a more *in vivo*-like phenotype when in the more physiologically relevant tri-culture.

We also exposed the iAst in mono-culture to the most highly expressed cytokines in the HIV-infected iMg, to determine whether the cytokines produced by infected iMg can elicit an inflammatory response in the iAst. We exposed the iAst to IL-1b and IL-8 at 10 ng/mL for 8 h and then analyzed the supernatants on the same six-cytokine panel. We found that, of the six cytokines tested, the iAst produced increased amounts of IL-1a (Figure S3B), suggesting that the iMicroglia can elicit an inflammatory response in the iAst.

We next sought to study iMg in an *in vitro* setting amenable to the study of synaptic phagocytosis and the influences of HIV and ART on gene expression in forebrain cells. To accomplish this we independently generated iNrn, iAst, and iMg cells, and then placed them in mixed cultures. For this study, analysis was performed 14 days after all 3 cell types are combined (Figure 3G), as our intention was to focus on the acute phase of exposure of forebrain-like neurons, astrocytes, and microglia to productively HIV-infected microglia. Having validated mono-cultures and assembled tri-cultures, we next used scRNA-seq to investigate cell-type-specific gene expression changes during infection ± EFZ.

scRNA-Seq Identified Each of the Three Cell Types in all Four Conditions

To create the tri-culture, we began the iNrn differentiation, added the iAst post-puromycin selection at D5 of the iNrn differentiation, and added the iMg at D7 of the iNrn differentiation, so that the iAst had time to acclimate before addition of HIV-infected iMg. The tri-culture was maintained for an additional 14 days, to D21 of the iNrn differentiation in NBM/B27 with neurotrophin 3 (NT-3) and brain-derived neurotrophic factor (BDNF) as described before (Zhang et al., 2013). To assay gene expression changes in each of the three cell types during HIV infection ± EFZ, we conducted scRNA-seq on four conditions: Uninf, Inf, Inf + EFZ, and Uninf + EFZ (Figure 4A). Cells were sequenced from the Uninf (n = 6,564), Inf (n = 7,431), Inf + EFZ (n = 7,111), and Uninf + EFZ (n = 10,071) conditions, with comparable numbers of each cell type per condition (Figure S5D). All conditions were then aggregated and initially analyzed through the Cellranger pipeline (10× Genomics, v.3.0.1). Secondary analysis was performed using the Seurat package in R. We generated 16 unbiased clusters (Figure 4B). First, we separated the clusters by cell type, then broke down each cell cluster by condition. We assigned clusters to one of the three cell types by expression of several key genes: iMg by expression of *IBA1*, *PU.1*, and *CD4*; iNrn by expression of *MAP2* and *SYN1*; and iAst by expression of *THBS1* and *SOX9* (Figures 4C–4E). There were four clusters (clusters 5, 10, 12, and 13) that did not fit into any of the three cell types by expression of the chosen markers (Figures 4B and 4F). To determine what the fourth cell type might represent, we examined the expression of the top 20 genes in each of the 4 cell types (Figure 4G). The gene expression pattern of the undesignated cells best matched the iAst, but scRNA-seq did not capture expression of THBS1 or SOX9, suggesting these cells represent less mature versions of the iAst. Hence, they were excluded from further analysis (Figure S5A). We then separated each cell type by condition (Figure S5B). We examined expression of genes related to inflammation and found the largest change in the iMg among the three cell types (Figure S5C).

Inflammatory Pathways and EIF2 Signaling Were Dysregulated among all Three Cell Types during Infection, but iMg Were Most Affected

To understand the gene expression changes among the three cell types during HIV infection ± EFZ, we first compared the Inf condition with Uninf. Several inflammatory pathways were significantly activated in Inf iMg compared with Uninf iMg, including IL-8 and NF-κB signaling. One of the top pathways dysregulated in Inf iMg compared with Uninf was the EIF2 pathway (Figure 5B). EIF2 signaling is involved in the UPR and, more broadly, the integrated stress response (ISR) (Janssens et al., 2014). The EIF2 pathway was not only dysregulated in iMg, but also was consistently increased in the iAst and iNrn (Figures S6A and S6B). However, only iMg had increased expression of *ATF4* mRNA, the transcription factor involved downstream of ISR activation (Masuda et al., 2013) in Uninf v Inf (Figure S5C). Previously, we have shown that the ISR, particularly the PERK arm, is activated in neurons and astrocytes from human brain samples with HAND (Akay et al., 2012; Lindl et al., 2007).

Inf + EFZ Caused Distinct Increased Activation of RhoGDI and CD40 Pathways

We next compared Uninf with Inf + EFZ, expecting to see a dampened immune response compared with Inf. Many of the top affected pathways in Inf iMg were related to inflammation, and there is a stark difference between Inf iMg and Inf + EFZ iMg (Figures 5B and 5D). However, the Inf + EFZ had a much milder inflammatory reaction, where RhoGDI and CD40 signaling were the only upregulated pathways compared with Uninf iMg (Figures 5D and 5E). RhoGDI negatively regulates Rac, which functions in multiple inflammation pathways (Wilkinson and Landreth, 2006), and CD40 activates NF-κB signaling (D'Aversa et al., 2008). A milder inflammatory response corroborates well with lesser disease severity seen in HAND patients who are taking ART (Saylor et al., 2016). Interestingly, EIF2 signaling was only activated in the iNrn in Inf + EFZ (Figures 5D, S6C, and S6D).

The scRNA-seq data suggest that the microglia were most affected by the infection ± EFZ, with major changes to EIF2 signaling, inflammatory, oxidative damage, and phagocytic gene pathways. However, the distinct activation of RhoGDI and CD40 in the Inf + EFZ condition suggests that the combination of Inf + EFZ creates a unique effect not seen with infection or EFZ alone.

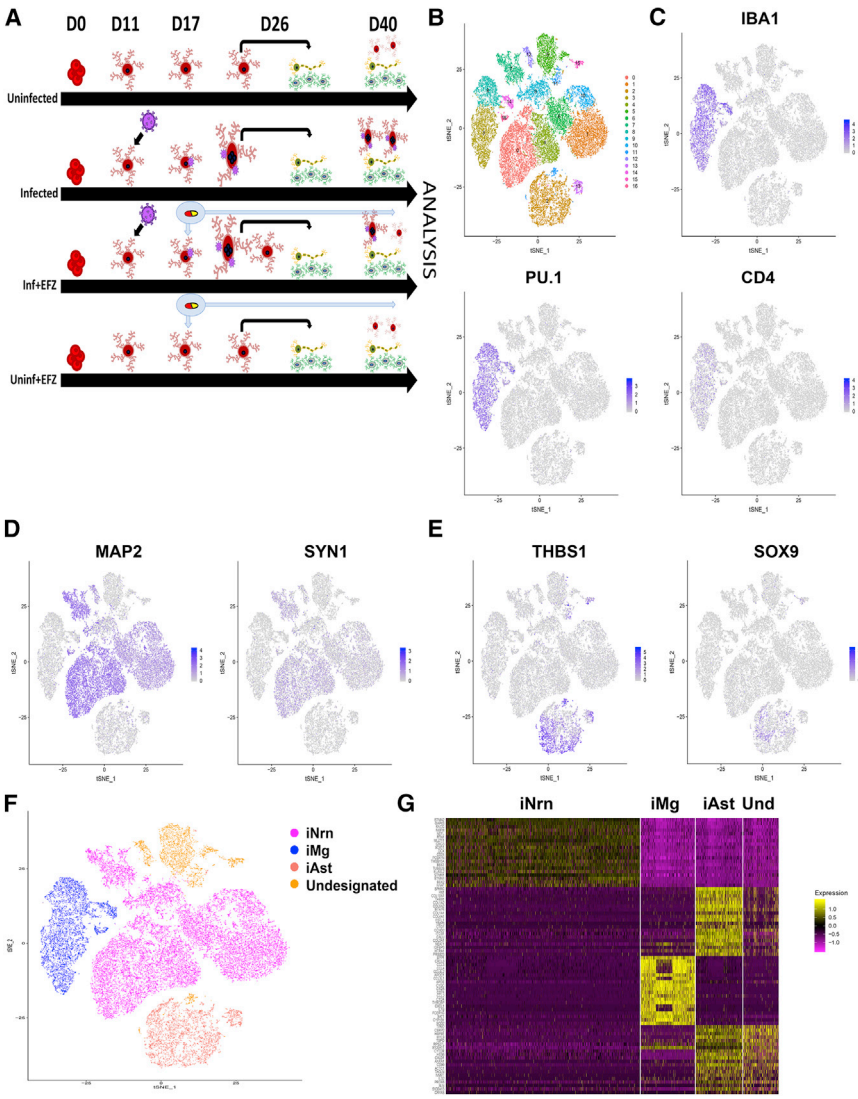

Figure 4. scRNA-Seq Identified Each of the Three Cell Types in all Four Conditions

(A) Timeline from start of CMP differentiation through tri-culture for the four conditions.

(B) t-SNE of unbiased clustering of combined scRNA-seq from all four conditions.

(C–E) Expression patterns of cell-type-specific markers for microglia (C), neurons (D), and astrocytes (E).

(F) t-SNE clustering by cell type based on cell-type-specific marker expression. One cluster did not align with any of the three cell types by the expression patterns chosen in (C–E).

(G) Heatmap of top 20 genes expressed in each cell type

Inf + EFZ Had an Attenuated, but Distinct Inflammatory Response Compared with Inf

Inf iMg had increased activity in several inflammatory pathways, including IL-6 signaling, neuroinflammation signaling, and Fcγ receptor-mediated phagocytosis compared with Inf + EFZ, suggesting that the Inf + EFZ had an overall lower immune response. However, the EIF2 signaling pathway, part of the ISR, was lower in Inf iMg compared with Inf + EFZ (Figure S6E).

Remarkably, EFZ treatment alone created distinct changes in immune-related signaling pathways in the iMg (Figure S6F), creating a unique cassette of dysregulated pathways not fully recapitulated in any other comparison with Uninf. These results show a stark difference in responses to EFZ treatment alone and EFZ treatment with infection, suggesting combinatorial and probably interacting effects of infection and EFZ treatment.

iMg Synaptophagocytosis Is Impaired in Inf, Inf + EFZ iMg, and Uninf + EFZ iMg

To further explore the differences in iMg responses to infection ± EFZ and EFZ treatment alone, we interrogated the ability of iMg to phagocytose synapses. Fcγ receptor-mediated phagocytosis pathway was activated in the Inf iMg as well as the Uninf + EFZ iMg compared with Uninf iMg (Figures 5B and S6F). In addition, HIV-infected macrophages and uninfected macrophages exposed to HIV display decreased phagocytic capabilities, specifically through the Fcγ receptor-mediated pathway, due to Nef and Tat inhibiting endocytosis (Debaisieux et al., 2015; Mazzolini et al.,

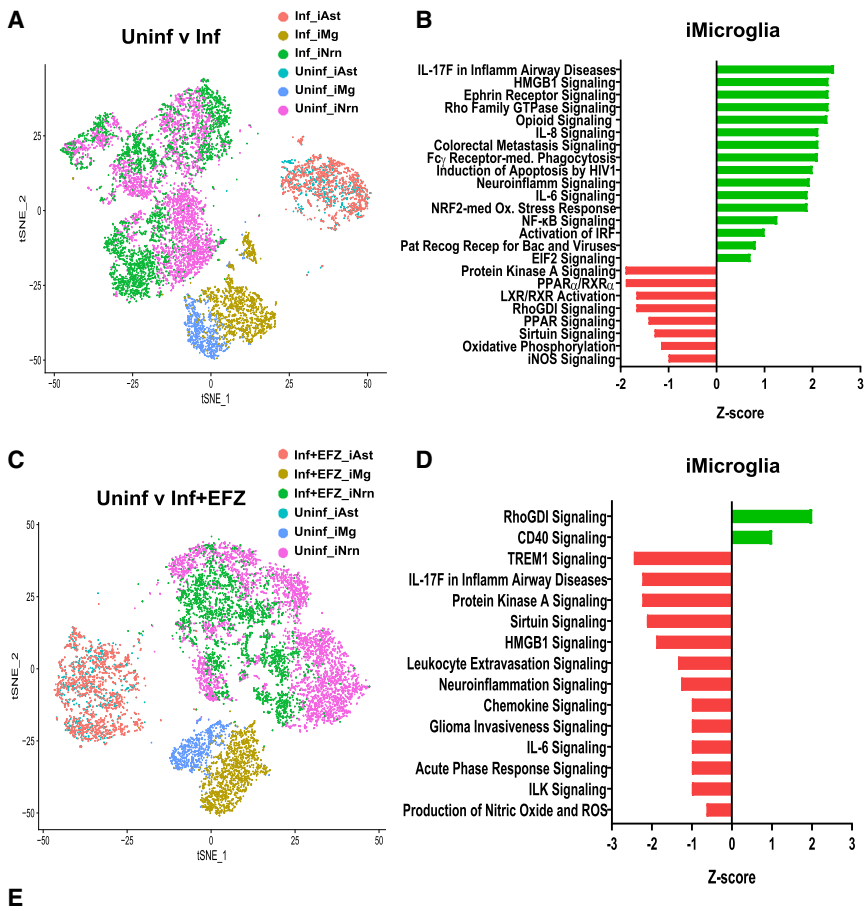

E

Pathway	Genes Dysregulated
RhoGDI Signaling	*RND3*, *CD44*, *ACTG1*, *PP1R12A*
CD40 Signaling	*NFKBIA*, *ICAM1*, *TNFAIP3*, *FOS*

Figure 5. iMg Activate RhoGDI and CD40 in Response to HIV Infection with EFZ Treatment

(A) t-SNE plot of Uninf and Inf conditions.

(B) Ingenuity Pathway Analysis of iMg between Uninf and Inf conditions. Uninf is baseline. Benjamini-Hochberg FDR = 0.05, Fisher's exact <0.05, *Z* score cutoff ±0.5.

(C) t-SNE plot of Uninf and Inf + EFZ conditions.

(D) Ingenuity Pathway Analysis of iMg between Uninf and Inf + EFZ conditions. Uninf is baseline. Benjamini-Hochberg FDR = 0.05, Fisher's exact <0.05, *Z* score cutoff ±0.5.

(E) Specific genes dysregulated that are involved in the RhoGDI and CD40 pathways in Inf + EFZ iMg compared with Uninf iMg. Red genes are downregulated. Green genes are upregulated.

2010). However, human microglia synaptophagocytosis in the context of HIV infection has not been tested.

In tri-cultures evaluated 14 days after addition of the iMg, we found colocalization of SYN1 in the LAMP1+ lysosomes of the iMg (Figures 6A and 6B), suggesting that the iMg phagocytize synaptic material. We confirmed that iMg are in contact with iNrn (Figure 6C), and importantly, only the iMg are infected as only they, and not the iNrn (Figure 6D) or iAst, show P24 immunofluorescence. In addition, 1 out of 1,208 iAst in the Inf condition had reads for p24 from the scRNA-seq. These results suggest that it is unlikely that astrocytes are productively infected but may internalize HIV particles from the infected microglia at very low levels. We were also able to delineate infected from uninfected iMg in the Inf + EFZ condition by multinucleation, which is present in nearly all P24 + iMg (Figures 2A and S7B).

The Inf iMg phagocytosed 70.9% less synapses than Uninf iMg ($p < 0.01$). In addition, in the Inf + EFZ condition, the infected (multinucleated) had 68.2% reduced phagocytosis ($p < 0.01$). However, the uninfected (single nucleated) iMg in the Inf + EFZ condition showed trends toward reduction in synaptophagy but was not statistically significant ($p = 0.1$). Finally, Uninf + EFZ condition iMg phagocytosed 57.1% less than Uninf iMg ($p < 0.05$) (Figures 6E and 6F). Multiple factors from the virus itself, the immune response, and the effects of antiretrovirals are acting on the iMg during HIV infection. All these factors may play a role in reducing synaptic phagocytosis and warrant future study.

To confirm that differences in apparent iMg synaptophagy are not secondary to reduced numbers of synapses overall in a given culture condition, we also measured local and random (50-μm radius areas with no iMg) synapse density to ensure the uninfected microglia were not in a more synapse dense area (Figures S7A and

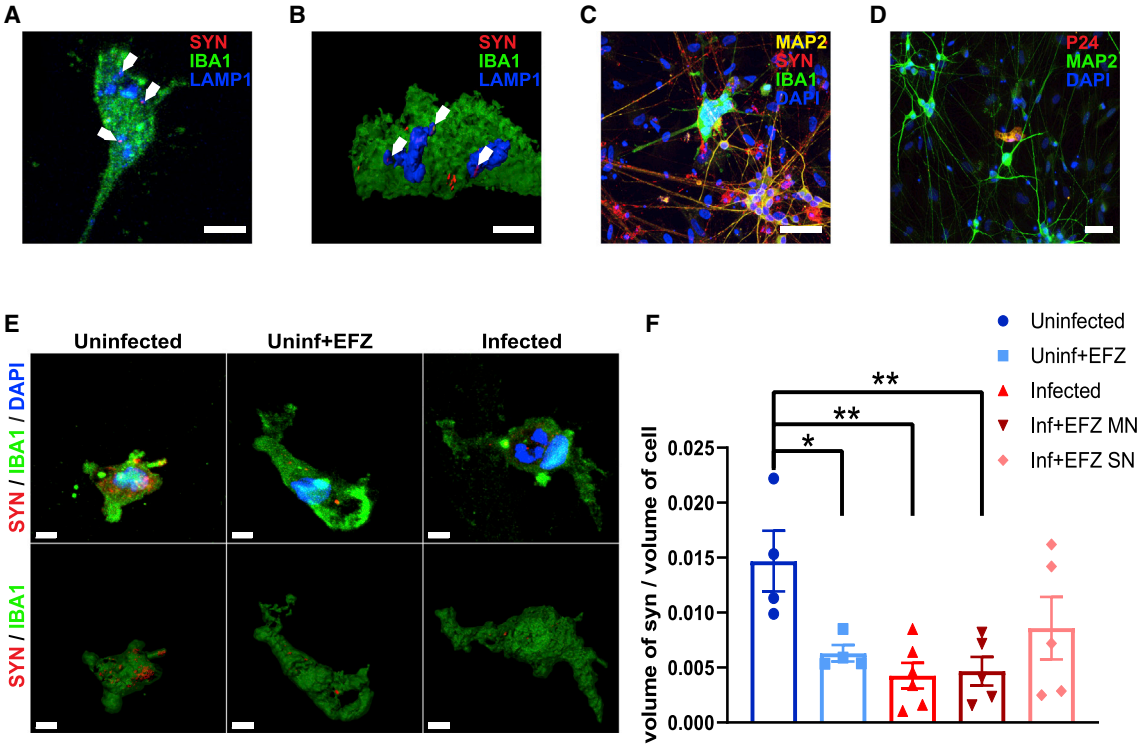

Figure 6. HIV-Infected iMicroglia Have Reduced Synaptophagocytosis, which Is Ameliorated by EFZ Treatment

(A and B) Immunostaining (A) and surface reconstruction of a side view (B) of iMg in an iNrn co-culture displaying synaptic phagocytosis by colocalization of synaptophysin+ (red) puncta within LAMP1+ (blue) lysosomes in IBA1+ (green) iMg. Sale bar represents 10 μm.

(C) Giant multinucleated IBA1+ (green) iMg potentially interacting with synaptophysin+ (red) synapses on MAP2+ (yellow) dendrites. Sale bar represents 50 μm.

(D) Multinucleated iMg, but not MAP2+ (green) iNrn or iAst, are P24+ (red) in the tri-culture after 14 days. Sale bar represents 50 μm.

(E) Representative surface reconstructions of synaptophysin signal (red) within IBA1+ (green) iMg in the Uninf, Uninf + EFZ, and Inf tri-cultures. SN, single nucleated; MN, multinucleated. Scale bar represents 5 μm.

(F) Synaptophagy is significantly decreased in infected iMg ± EFZ and uninfected iMg + EFZ compared with control. n = 4 (Uninf = 4, Uninf + EFZ = 4, Inf = 6, Inf + EFZ = 6) independent differentiations of WT6, one-way ANOVA, Dunnett's post hoc analysis; *$p < 0.05$; error bars represent SEM.

S7C). In fact, there was no significant difference in iMg-proximal or random synapse density across all conditions (Figures S7D and S7E). This finding aligns with previous studies that demonstrate inhibition of phagocytosis by viral proteins Tat and Nef in both infected and uninfected macrophages (Debaisieux et al., 2015; Mazzolini et al., 2010) and is also consistent with ART-related impairment of phagocytosis (Giunta et al., 2011).

EFZ Reduced the Production of IL-8 and IL-1b by Infected iMg, but Enhanced TNF-α

To validate the activation of cytokine and inflammatory pathways in infected microglia ± EFZ, we compared cytokine production between each condition in tri-culture. Starting at the time of iMg addition, we collected supernatant every 5 days until day 14 of tri-culture. Reverse transcriptase activity confirmed that the iMg in the infected condition remain productively infected (Figure 7A). IL-8 and IL-1b were significantly increased in the infected tri-culture compared with uninfected control 5 days after iMg introduction ($p < 0.0001$, $p < 0.001$). IL-1b remained increased over uninfected at each time point; however, IL-8 decreases by day 10 (Figures 7B and 7C). The Inf + EFZ condition had consistent, significant reduced cytokine production of IL-8 from D10 through D14 ($p < 0.0001$) and IL-1b at D5 ($p < 0.01$) compared with Uninf. Uninf + EFZ had the lowest levels of cytokine production across all the groups (Figures 7B–7D). In addition, there was no increase in TNF-α in the Inf tri-culture. However, the Inf + EFZ condition did have increased TNF-α compared with all other conditions at D5 (Figure 7D). The Inf and Inf + EFZ tri-cultures also did not exhibit increases in IL-6 or IL-10, similar to our

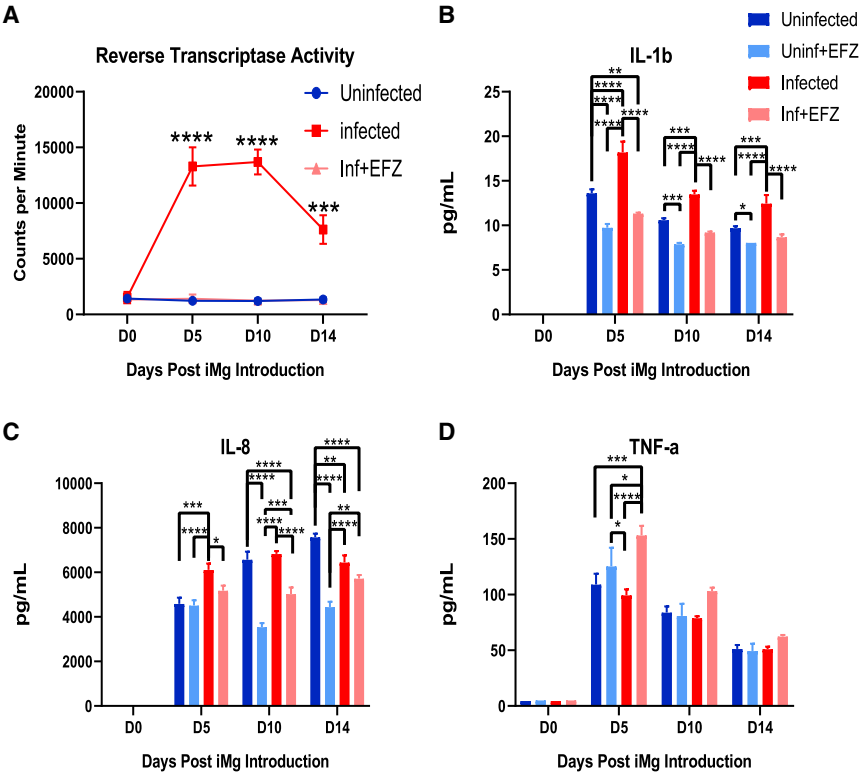

Figure 7. Inf + EFZ Mitigates IL-1b and IL-8 Production, but Increases TNF-α Production

(A) Reverse transcriptase activity of Uninf, Inf, and Inf + EFZ tri-culture. n = 3 infections of WT6, one-way ANOVA, Dunnett's post hoc analysis; ***p < 0.001, ****p < 0.0001; error bars represent SEM.

(B–D) Cytokine analysis of Uninf, Uninf + EFZ, Inf, and Inf + EFZ iMg displays increase in IL-1b (B) and IL-8 (C) production in the Inf tri-culture, and Inf + EFZ had increased TNF-α (D). n = 3 infections of WT6, two-way ANOVA, Tukey's post hoc analysis; *p < 0.05, **p < 0.01, ***p < 0.001, ****p < 0.0001; error bars represent SEM.

culture findings (Figures S2H and S2I). These data combined with the scRNA data suggest there are distinct influences on the inflammatory response during infection alone and infection with EFZ. Inf iMg exclusively had increased expression of *CXCL8* and *IL1B* genes (Figure S5C). In addition, IL-8 and NF-κB signaling were activated only in Inf iMg compared with Uninf by scRNA-seq (Figure 5B) Interestingly, TNF-α regulates *AP-1* (*FOS*) (Clark et al., 2005), a CD40 signaling pathway gene that is upregulated in Inf + EFZ iMg when compared with the Uninf (Figures S5C and 5D). These results further suggest distinct inflammatory reactions from Inf and Inf + EFZ that are observed in the iMg.

DISCUSSION

We describe an hiPSC tri-culture model to investigate the interdependent and individual roles of microglia, astrocytes, and neurons in the context of HIV infection. In recent years, there have been several new differentiation protocols for these cell types (Abud et al., 2017; Santos et al., 2017; Zhang et al., 2013) and several iPSC/primary cell co-cultures that have studied various neurological disorders (Lin et al., 2018; Park et al., 2018). This model advances previous works in exploring gene expression changes with scRNA-seq in the context of viral infection and relevant drug treatments to begin to unfurl a particularly difficult disease to study.

This model recapitulates several previous *in vivo* findings, such as increases in IL-8 and IL-1b production in microglia and EIF2 signaling in astrocytes and neurons (Akay et al., 2012; Ginsberg et al., 2018). The consistent activation of EIF2 signaling in all three cell types not only recapitulates previous findings, but also suggests microglia have dysregulated EIF2 signaling. ISR and EIF2 activation has been implicated in establishing initial viral replication (Jiang et al., 2017). A recent study also found stress response genes, including the ISR-associated gene *ATF4*, upregulated in the brains of older HIV-positive patients (Solomon et al., 2019). The UPR and consequently EIF2 activation has been implicated in multiple neurodegenerative disorders (Scheper and Hoozemans, 2015), these findings bolster the possibility that UPR and ISR activation play important roles in HAND development or at least the initial response to HIV in the brain.

We also found that the gene pathways associated with IL-8, IL-1b, and TNF-α production were upregulated in iMg, suggesting that the microglia are the main culprit in the initial response to HIV infection. However, iMg infection seems to lead to reduced phagocytosis of synapses. This falls in line with previously reported impaired phagocytosis

by HIV-infected or exposed macrophages (Debaisieux et al., 2015; Mazzolini et al., 2010). While random synapse density was variable, there was consistent reduced synaptic particles in Inf iMg, suggesting that there was reliably a surplus of synapses. Although not significant, Uninf + EFZ cultures had consistently less overall synapse density, suggesting that the reduced phagocytosis may be due to a global reduction in synapses. In addition, we cannot rule out the possibility that the Inf or Uninf + EFZ were more efficient in degrading the synaptic particles. Ideally, future studies using live-imaging are warranted to resolve this issue. How iMg phagocytosis would be affected or if inflammation patterns would change in longer-term cultures remain to be determined.

In addition, we discovered a starkly different immune response at the gene and functional level in Inf versus Inf + EFZ, characterized by distinct CD40/RhoGDI pathway activation and TNF-α production. CD40 and RhoGDI activation could be controlled by the increased production of TNF-α that was only found in the Inf + EFZ condition. This persistent immune activation highlights the need for further studies into the role that antiretrovirals play in propagating the chronic inflammation seen in HIV patients today (Kolson, 2017). The mitigated reaction we observed with EFZ treatment is consistent with human studies showing a reduced severity of HAND with the widespread use of antiretroviral therapies (Saylor et al., 2016), but also with its persistence despite control of viral load. Furthermore, we revealed a substantial immune response to EFZ treatment alone. This warrants further study, particularly due to the recommended prophylactic use of ART in HIV-negative patients (Spinner et al., 2016).

hiPSC cultures are particularly useful for studying HIV neuropathology, since human primary neuronal cells and postmortem tissue are limited in availability and not amenable to molecular manipulation. In addition, HIV only infects human cells, rendering the interpretation of results from animal models more convoluted. Hence, mechanistic studies of the influences of HIV and ART on human neural cells are limited. This tri-culture system allows us to better study the mechanisms of early HIV infection in the brain. However, there are caveats to this system that must be considered. Each of the iPSC-derived cell types are similar to their *in vivo* counterparts by gene and protein expression, as well as function, but are not exact. In addition, the iCells' gene expression profile at the end stage of differentiation is relatively immature and more closely represents early stages of development *in vivo*. Still, our culture system allows reductionist study of three key cell types over weeks of infection, but it may be refined by inclusion of additional cell types to further optimize modeling HAND in the adult and/or chronic setting.

This tri-culture has validated several findings in the field, as well as, produced multiple findings for HIV neuropathology. However, this model is not restricted to HIV neuropathology and can also be utilized to study other neurological disorders. This highly tractable, reductive system can be genetically and pharmacologically modified at any stage. These differentiations could also be used on patient-derived cells, creating a disease-relevant, patient-specific tri-culture system. Similar cultures have been developed (Haenseler et al., 2017; Park et al., 2018), but not to this complexity or with a focus on viral infections. The innovation of the tri-culture is not the individual differentiations of iMg or iAst, as there are many published differentiations. Rather, it is an all hiPSC tri-culture that reliably recapitulated the intricate interactions among multiple cell types during HIV infection and revealed new, potential therapeutic targets. Alternatively differentiated iNrn, iMg, or iAst or additional cell types could be implemented. The tri-culture can be another instrumental tool in understanding the workings of complex neurological disorders and in developing novel therapeutic strategies.

EXPERIMENTAL PROCEDURES

iNeuron Differentiation of iPSCs

iPSCs were transfected with two plasmids VSVG.HIV.SIN.cPPT.CMV.mNgn2.WPRE and VSVG.HIV.SIN.cPPT.CMV.rTTA.WPRE, produced by Marius Wernig (Stanford University) and packaged by the University of Pennsylvania Viral Vector Core. Cells were exposed to 1 μg/mL polybrene (Sigma-Aldrich TR-1003). The medium is fully exchanged 6 h after exposure. iPSCs are differentiated according to a previously published method (Zhang et al., 2013). In brief, after transfection, iPSCs were exposed to N2 medium containing 5 mL N2 Supplement-B (STEMCELL Technologies 07156), 0.5 mL 55 mM β-mercaptoethanol (Life Technologies 21985-023), 0.5 mL primocin (Invivogen ant-pm-2), BDNF (10 ng/mL, PeproTech 450-02), NT-3 (10 ng/mL, PeproTech 450-03), laminin (200 ng/mL, Sigma L2020), and doxycycline (2 μg/mL, Sigma D3072) in DMEM/F12 (Gibco 11,320-033) for 24 h (DIV0). Cells were then exposed to puromycin (5 μg/mL, Sigma P9620) for 24 h in the same N2 medium (DIV1). iNeurons were re-plated 24 h later (DIV2) to experiment-appropriate plates coated with Matrigel GFR (Corning 354230) (1:20 DMEM). Cells were washed 2× in PBS and lifted with StemPro accutase (Thermo Fisher Scientific, A11105-01) for 5 min at 37°C. Cells were spun down at 1,000 rpm for 5 min at room temperature. Cells were resuspended and plated in iN medium (Neurobasal-A medium; Invitrogen, A24775-01) with 5 mM glucose (Sigma, G5146), 10 mM sodium pyruvate (Sigma, P5280), glutamax (Life Technologies, 35050-061), penicillin/streptomycin (Thermo Fisher Scientific, 15140-148), BDNF and NT-3 (10 ng/mL), and doxycycline (2 μg/mL) through 9 days. Ara-C (2 μM, Sigma, C6645) was added on DIV3, and there was a full medium exchange 24 h later (DIV4). Doxycycline was discontinued at DIV10 for the rest of the 21-day differentiation.

iAstrocyte Differentiation of iPSCs

iPSCs transfected with the NGN2 virus were put through the first 2 days of the iNeuron differentiation. On day 3, cells were exposed to astrocyte differentiation medium: N2 medium (without BDNF, NT-3, laminin, and doxycycline), 10% FBS (HyClone SH30071.03HI), B-27 with vitamin A (Thermo Fisher Scientific, 17504044), FGF-2 (20 ng/mL, R&D Systems, 233-FB-025) and EGF (20 ng/mL, R&D Systems, 236-EG-200). After 30 days, EGF was removed and FGF2 reduced to 5 ng/mL. After 70 total days, cells were switched into Astrocyte Medium (Sciencell, 1801). Experiments were performed after 90 total days of differentiation.

iMicroglia Differentiation of iPSCs

iPSCs were differentiated into CMPs according to the published protocol (Paluru et al., 2014) by the Human Pluripotent Stem Cell Core (CHOP). CMPs were plated at 333k cells/well in a 24-well CellBIND plate (Corning 3337). CMPs were differentiated in iMg medium (RPMI 1640 medium, GE Healthcare Life Sciences, SH30027.01) with 10% FBS (HyClone, SH30071.03HI), recombinant human IL-34 (100 ng/mL, R&D Systems, 5265-IL-010), CSF-1 recombinant human protein (25 ng/mL, Thermo Fisher Scientific, PHC9504), and recombinant human TGF-β1 (50 ng/mL, PeproTech, 100-21). Half medium changes were performed every 2 days for 11 days.

Tri-culture Combination

iNeurons were differentiated as described above and re-plated on DIV2 to Matrigel (Corning, 354230) coated (1:20 DMEM) Nunc Lab-Tek II 8-well chamber slides (Thermo Fisher Scientific, 62407-296) at 70k cells/well in iN medium. On DIV5 of iNeuron differentiation, the iAstrocytes were added at 50k cells/well. On DIV7 of iNeuron differentiation, iMicroglia were added at 100k cells/well. Cultures were taken out to DIV21 of iNeuron differentiation.

Statistics

GraphPad Prism 8 was used for statistical analysis. One-way ANOVA and Dunnett's post hoc, two-way ANOVA and Tukey's post hoc, two-way ANOVA and Sidak's post hoc, two-tailed t test, or two-tailed paired t test were used as indicated. p values are indicated in figures as *$p < 0.05$, **$p < 0.01$, ***$p < 0.001$, ****$p < 0.0001$; n.s., not significant.

ACCESSION NUMBERS

The datasets generated during and/or analyzed during this study are available in the GEO repository https://www.ncbi.nlm.nih.gov/geo/query/acc.cgi?acc=GSE143687. The accession number for the data reported in this paper is GEO:GSE143687.

SUPPLEMENTAL INFORMATION

Supplemental Information can be found online at https://doi.org/10.1016/j.stemcr.2020.02.010.

AUTHOR CONTRIBUTIONS

Conceptualization, S.A.A., K.L.J.-S., and S.K.R.; Methodology, S.A.A., K.L.J.-S., and S.K.R.; Investigation, S.K.R.; Formal Analysis, S.K.R., M.V.G., N.P.S., and J.P.G.; Writing – Original Draft, S.K.R., S.A.A., K.L.J.-S., F.C.B., and K.S.W.; Funding Acquisition, S.A.A. and K.L.J.-S.; Resources, S.A.A., K.L.J.-S., F.C.B., and H.H.; Supervision, K.J.S. and S.A.A.

ACKNOWLEDGMENTS

This work was supported by the National Institute of Neurological Disorders and Stroke (R21 NS107594 02) and the Penn Center for Aids Research (CFAR) and Penn Mental Health AIDS Research Center (PMHARC) (5-P30-MH-097488-05). We thank the Human Pluripotent Stem Cell Core (CHOP) for providing CMPs, Center for Applied Genomics for performing and analyzing RNA-seq, CFAR for providing HIV strains, and PMHARC for analyzing cytokines. We thank Elizabeth Krizman for performing western blots and glutamate uptake assays, who was partially supported by the Intellectual and Developmental Disabilities Research Center at CHOP/Penn U54 HD086984, and Herbert M. Lachman, MD, for providing iPSC lines.

Received: October 25, 2019
Revised: February 24, 2020
Accepted: February 25, 2020
Published: March 26, 2020

REFERENCES

Abud, E.M., Ramirez, R.N., Martinez, E.S., Healy, L.M., Nguyen, C.H.H., Newman, S.A., Yeromin, A.V., Scarfone, V.M., Marsh, S.E., Fimbres, C., et al. (2017). iPSC-derived human microglia-like cells to study neurological diseases. Neuron *94*, 278–293.e9.

Akay, C., Lindl, K.A., Shyam, N., Nabet, B., Goenaga-Vazquez, Y., Ruzbarsky, J., Wang, Y., Kolson, D.L., and Jordan-Sciutto, K.L. (2012). Activation status of integrated stress response pathways in neurones and astrocytes of HIV-associated neurocognitive disorders (HAND) cortex. Neuropathol. Appl. Neurobiol. *38*, 175–200.

Castellano, P., Prevedel, L., and Eugenin, E.A. (2017). HIV-infected macrophages and microglia that survive acute infection become viral reservoirs by a mechanism involving Bim. Sci. Rep. *7*, 12866.

Chen, W., Sulcove, J., Frank, I., Jaffer, S., Ozdener, H., and Kolson, D.L. (2002). Development of a human neuronal cell model for human immunodeficiency virus (HIV)-infected macrophage-induced neurotoxicity: apoptosis induced by HIV type 1 primary isolates and evidence for involvement of the Bcl-2/Bcl-xL-sensitive intrinsic apoptosis pathway. J. Virol. *76*, 9407–9419.

Christopherson, K.S., Ullian, E.M., Stokes, C.C., Mullowney, C.E., Hell, J.W., Agah, A., Lawler, J., Mosher, D.F., Bornstein, P., and Barres, B.A. (2005). Thrombospondins are astrocyte-secreted proteins that promote CNS synaptogenesis. Cell *120*, 421–433.

Ciccarelli, N., Fabbiani, M., Di Giambenedetto, S., Fanti, I., Baldonero, E., Bracciale, L., Tamburrini, E., Cauda, R., De Luca, A., and Silveri, M.C. (2011). Efavirenz associated with cognitive disorders in otherwise asymptomatic HIV-infected patients. Neurology *76*, 1403.

Clark, J., Vagenas, P., Panesar, M., and Cope, A.P. (2005). What does tumour necrosis factor excess do to the immune system long term? Ann. Rheum. Dis. *64* (suppl 4), iv70.

D'Aversa, T.G., Eugenin, E.A., and Berman, J.W. (2008). CD40-CD40 ligand interactions in human microglia induce CXCL8 (interleukin-8) secretion by a mechanism dependent on activation of ERK1/2 and nuclear translocation of nuclear factor-kappaB (NFkappaB) and activator protein-1 (AP-1). J. Neurosci. Res. *86*, 630–639.

De Clercq, E. (2004). Non-nucleoside reverse transcriptase inhibitors (NNRTIs): past, present, and future. Chem. Biodivers. *1*, 44–64.

Debaisieux, S., Lachambre, S., Gross, A., Mettling, C., Besteiro, S., Yezid, H., Henaff, D., Chopard, C., Mesnard, J.M., and Beaumelle, B. (2015). HIV-1 Tat inhibits phagocytosis by preventing the recruitment of Cdc42 to the phagocytic cup. Nat. Commun. *6*, 6211.

Deng, H., Liu, R., Ellmeier, W., Choe, S., Unutmaz, D., Burkhart, M., Di Marzio, P., Marmon, S., Sutton, R.E., Hill, C.M., et al. (1996). Identification of a major co-receptor for primary isolates of HIV-1. Nature *381*, 661–666.

Easley-Neal, C., Foreman, O., Sharma, N., Zarrin, A.A., and Weimer, R.M. (2019). CSF1R ligands IL-34 and CSF1 are differentially required for microglia development and maintenance in white and gray matter brain regions. Front. Immunol. *10*, 2199.

Ginsberg, S.D., Alldred, M.J., Gunnam, S.M., Schiroli, C., Lee, S.H., Morgello, S., and Fischer, T. (2018). Expression profiling suggests microglial impairment in human immunodeficiency virus neuropathogenesis. Ann. Neurol. *83*, 406–417.

Giunta, B., Ehrhart, J., Obregon, D.F., Lam, L., Le, L., Jin, J., Fernandez, F., Tan, J., and Shytle, R.D. (2011). Antiretroviral medications disrupt microglial phagocytosis of β-amyloid and increase its production by neurons: implications for HIV-associated neurocognitive disorders. Mol. Brain *4*, 23.

Gosselin, D., Skola, D., Coufal, N.G., Holtman, I.R., Schlachetzki, J.C.M., Sajti, E., Jaeger, B.N., O'Connor, C., Fitzpatrick, C., Pasillas, M.P., et al. (2017). An environment-dependent transcriptional network specifies human microglia identity. Science *356*. https://doi.org/10.1126/science.aal3222.

Haenseler, W., Sansom, S.N., Buchrieser, J., Newey, S.E., Moore, C.S., Nicholls, F.J., Chintawar, S., Schnell, C., Antel, J.P., Allen, N.D., et al. (2017). A highly efficient human pluripotent stem cell microglia model displays a neuronal-co-culture-specific expression profile and inflammatory response. Stem Cell Reports *8*, 1727–1742.

Janssens, S., Pulendran, B., and Lambrecht, B.N. (2014). Emerging functions of the unfolded protein response in immunity. Nat. Immunol. *15*, 910–919.

Jiang, G., Santos Rocha, C., Hirao, L.A., Mendes, E.A., Tang, Y., Thompson, G.R., 3rd, Wong, J.K., and Dandekar, S. (2017). HIV exploits antiviral host innate GCN2-ATF4 signaling for establishing viral replication early in infection. MBio *8*. https://doi.org/10.1128/mBio.01518-16.

Kang, P., Lee, H.K., Glasgow, S.M., Finley, M., Donti, T., Gaber, Z.B., Graham, B.H., Foster, A.E., Novitch, B.G., Gronostajski, R.M., et al. (2012). Sox9 and NFIA coordinate a transcriptional regulatory cascade during the initiation of gliogenesis. Neuron *74*, 79–94.

Kim, B.O., Liu, Y., Ruan, Y., Xu, Z.C., Schantz, L., and He, J.J. (2003). Neuropathologies in transgenic mice expressing human immunodeficiency virus type 1 Tat protein under the regulation of the astrocyte-specific glial fibrillary acidic protein promoter and doxycycline. Am. J. Pathol. *162*, 1693–1707.

Kolson, D. (2017). Neurologic complications in persons with HIV infection in the era of antiretroviral therapy. Top. Antivir. Med. *25*, 97–101.

Lin, Y.-T., Seo, J., Gao, F., Feldman, H.M., Wen, H.-L., Penney, J., Cam, H.P., Gjoneska, E., Raja, W.K., Cheng, J., et al. (2018). APOE4 causes widespread molecular and cellular alterations associated with Alzheimer's disease phenotypes in human iPSC-derived brain cell types. Neuron *98*, 1141–1154.e7.

Lindl, K.A., Akay, C., Wang, Y., White, M.G., and Jordan-Sciutto, K.L. (2007). Expression of the endoplasmic reticulum stress response marker, BiP, in the central nervous system of HIV-positive individuals. Neuropathol. Appl. Neurobiol. *33*, 658–669.

Liu, R., Paxton, W.A., Choe, S., Ceradini, D., Martin, S.R., Horuk, R., MacDonald, M.E., Stuhlmann, H., Koup, R.A., and Landau, N.R. (1996). Homozygous defect in HIV-1 coreceptor accounts for resistance of some multiply-exposed individuals to HIV-1 infection. Cell *86*, 367–377.

Masuda, M., Miyazaki-Anzai, S., Levi, M., Ting, T.C., and Miyazaki, M. (2013). PERK-eIF2alpha-ATF4-CHOP signaling contributes to TNFalpha-induced vascular calcification. J. Am. Heart Assoc. *2*, e000238.

Mazzolini, J., Herit, F., Bouchet, J., Benmerah, A., Benichou, S., and Niedergang, F. (2010). Inhibition of phagocytosis in HIV-1-infected macrophages relies on Nef-dependent alteration of focal delivery of recycling compartments. Blood *115*, 4226–4236.

Michler-Stuke, A., Wolff, J.R., and Bottenstein, J.E. (1984). Factors influencing astrocyte growth and development in defined media. Int. J. Dev. Neurosci. *2*, 575–584.

O'Donnell, L.A., Agrawal, A., Jordan-Sciutto, K.L., Dichter, M.A., Lynch, D.R., and Kolson, D.L. (2006). Human immunodeficiency virus (HIV)-induced neurotoxicity: roles for the NMDA receptor subtypes. J. Neurosci. *26*, 981–990.

Paluru, P., Hudock, K.M., Cheng, X., Mills, J.A., Ying, L., Galvão, A.M., Lu, L., Tiyaboonchai, A., Sim, X., Sullivan, S.K., et al. (2014). The negative impact of Wnt signaling on megakaryocyte and primitive erythroid progenitors derived from human embryonic stem cells. Stem Cell Res. *12*, 441–451.

Park, J., Wetzel, I., Marriott, I., Dréau, D., D'Avanzo, C., Kim, D.Y., Tanzi, R.E., and Cho, H. (2018). A 3D human triculture system modeling neurodegeneration and neuroinflammation in Alzheimer's disease. Nat. Neurosci. https://doi.org/10.1038/s41593-018-0175-4.

Santos, R., Vadodaria, K.C., Jaeger, B.N., Mei, A., Lefcochilos-Fogelquist, S., Mendes, A.P.D., Erikson, G., Shokhirev, M., Randolph-Moore, L., Fredlender, C., et al. (2017). Differentiation of inflammation-responsive astrocytes from glial progenitors generated from human induced pluripotent stem cells. Stem Cell Reports *8*, 1757–1769.

Saylor, D., Dickens, A.M., Sacktor, N., Haughey, N., Slusher, B., Pletnikov, M., Mankowski, J.L., Brown, A., Volsky, D.J., and McArthur, J.C. (2016). HIV-associated neurocognitive disorder—pathogenesis and prospects for treatment. Nat. Rev. Neurol. *12*, 234–248.

Scheper, W., and Hoozemans, J.J. (2015). The unfolded protein response in neurodegenerative diseases: a neuropathological perspective. Acta Neuropathol. *130*, 315–331.

Shah, A., Verma, A.S., Patel, K.H., Noel, R., Rivera-Amill, V., Silverstein, P.S., Chaudhary, S., Bhat, H.K., Stamatatos, L., Singh, D.P., et al. (2011). HIV-1 gp120 induces expression of IL-6 through a nuclear factor-kappa B-dependent mechanism: suppression by gp120 specific small interfering RNA. PLoS One *6*, e21261.

Solomon, I.H., Chettimada, S., Misra, V., Lorenz, D.R., Gorelick, R.J., Gelman, B.B., Morgello, S., and Gabuzda, D. (2019). White matter abnormalities linked to interferon, stress response, and energy metabolism gene expression changes in older HIV-positive patients on antiretroviral therapy. Mol. Neurobiol. https://doi.org/10.1007/s12035-019-01795-3.

Spinner, C.D., Boesecke, C., Zink, A., Jessen, H., Stellbrink, H.-J., Rockstroh, J.K., and Esser, S. (2016). HIV pre-exposure prophylaxis (PrEP): a review of current knowledge of oral systemic HIV PrEP in humans. Infection *44*, 151–158.

Sui, Z., Sniderhan, L.F., Schifitto, G., Phipps, R.P., Gelbard, H.A., Dewhurst, S., and Maggirwar, S.B. (2007). Functional synergy between CD40 ligand and HIV-1 Tat contributes to inflammation: implications in HIV type 1 dementia. J. Immunol. *178*, 3226–3236.

Swanson, R.A., Liu, J., Miller, J.W., Rothstein, J.D., Farrell, K., Stein, B.A., and Longuemare, M.C. (1997). Neuronal regulation of glutamate transporter subtype expression in astrocytes. J. Neurosci. *17*, 932–940.

Taramasso, L., Biagio, A.D., Maggiolo, F., Tavelli, A., Caputo, S.L., Bonora, S., Zaccarelli, M., Caramello, P., Costantini, A., Viscoli, C., et al. (2018). First-line antiretroviral therapy with efavirenz plus tenofovir disiproxil fumarate/emtricitabine or rilpivirine plus tenofovir disiproxil fumarate/emtricitabine: a durability comparison. HIV Med. *19*, 475–484.

Turchan–Cholewo, J., Dimayuga, V.M., Gupta, S., Gorospe, R.M.C., Keller, J.N., and Bruce–Keller, A.J. (2009). NADPH oxidase drives cytokine and neurotoxin release from microglia and macrophages in response to HIV-Tat. Antioxid. Redox Signal. *11*, 193–204.

Wilkinson, B.L., and Landreth, G.E. (2006). The microglial NADPH oxidase complex as a source of oxidative stress in Alzheimer's disease. J. Neuroinflammation *3*, 30.

Zhang, Y., Pak, C., Han, Y., Ahlenius, H., Zhang, Z., Chanda, S., Marro, S., Patzke, C., Acuna, C., Covy, J., et al. (2013). Rapid single-step induction of functional neurons from human pluripotent stem cells. Neuron *78*. https://doi.org/10.1016/j.neuron.2013.05.029.

Stem Cell Reports, Volume *14*

Supplemental Information

Neuroinflammation and EIF2 Signaling Persist despite Antiretroviral Treatment in an hiPSC Tri-culture Model of HIV Infection

Sean K. Ryan, Michael V. Gonzalez, James P. Garifallou, Frederick C. Bennett, Kimberly S. Williams, Nathaniel P. Sotuyo, Eugene Mironets, Kieona Cook, Hakon Hakonarson, Stewart A. Anderson, and Kelly L. Jordan-Sciutto

Supplemental Data

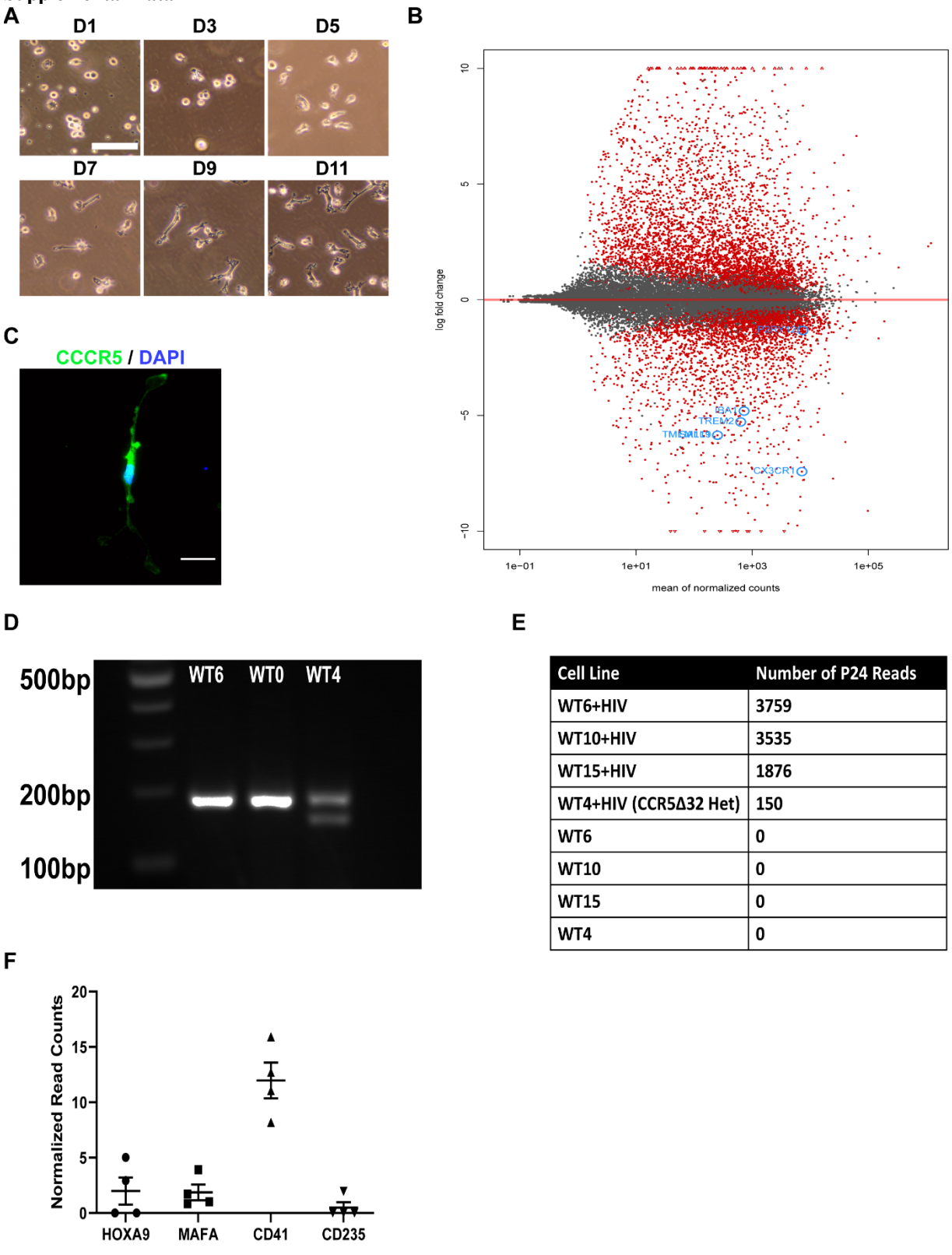

Cell Line	Number of P24 Reads
WT6+HIV	3759
WT10+HIV	3535
WT15+HIV	1876
WT4+HIV (CCR5Δ32 Het)	150
WT6	0
WT10	0
WT15	0
WT4	0

Figure S1: iMg and CCR5Δ32 mutation characterization. Related to Figures 1 and 2
(A) Brightfield images of iMg differentiation, depicting ramification by D11. Scale bar represents 50µm.

(B) MA plot of bulk RNAseq data comparing iMg (baseline) to MDMs. n=3 Benjamini-Hochberg FDR-0.05.
(C) Immunostaining showing CCR5 expression (green) on D11 iMg. Scale bar represents 25um.
(D) PCR of CCR5Δ32 shows WT4 is heterozygous for the mutation.
(E) Infected WT4 has dramatically less raw reads of P24 from Bulk RNAseq compared to infected WT6 and WT10 iMg.
(F) Normalized read counts showing lack of expression of myeloid progenitor markers in iMg bulk RNAseq. n=4 cell lines. Error bars represent SEM.

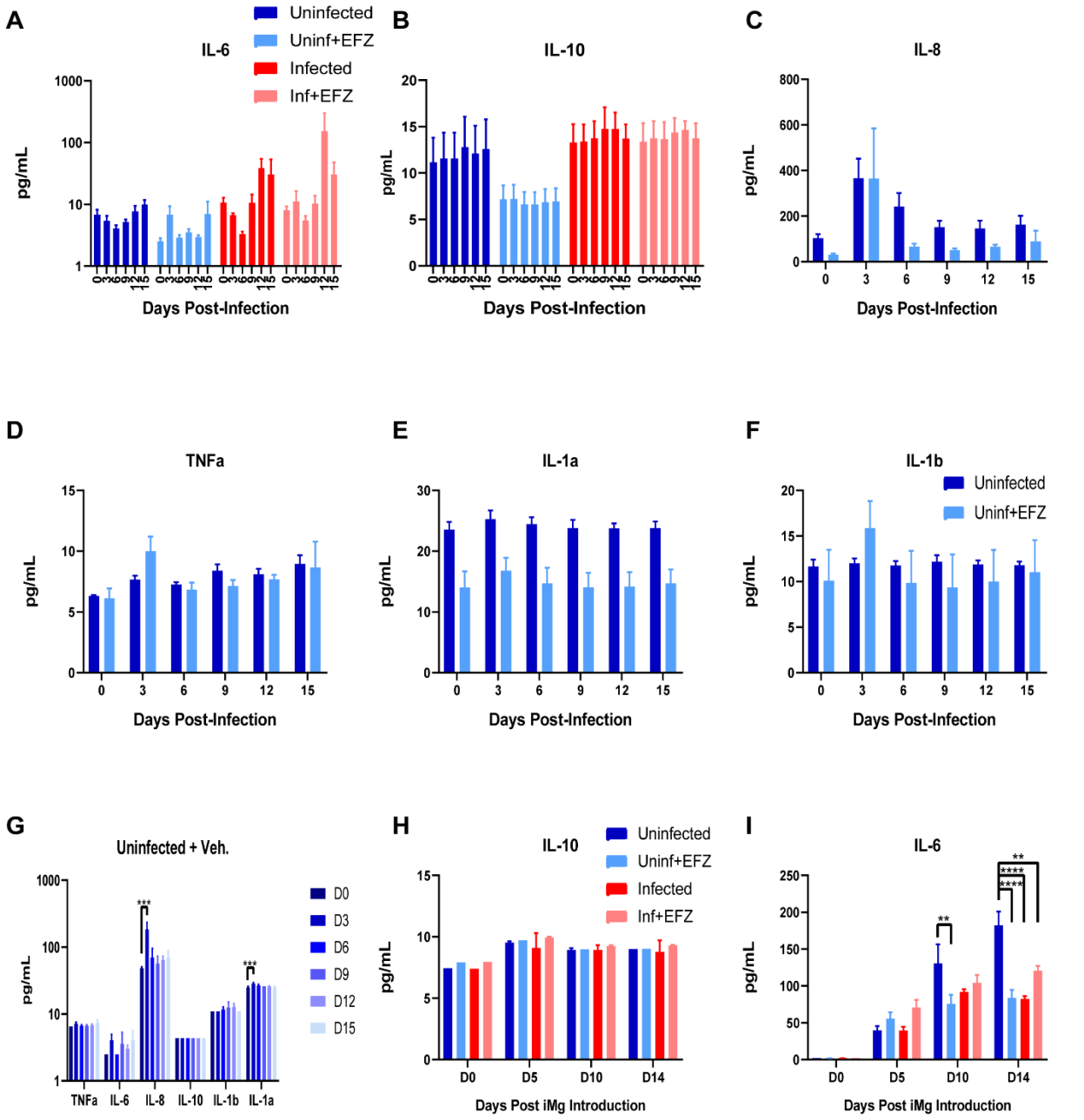

Figure S2: Additional cytokine expression during infection and with vehicle control. Related to Figures 2 and 7

(A&B) IL-6 (A) and IL-10 (B) production in mono-culture did not change for any of the four conditions. n=3 independent differentiations of WT6 (n=4 Uninf and Uninf+EFZ, n=3 Inf and Inf+EFZ), one-way ANOVA, Dunnett's post hoc analysis, error bars represent SEM.

(C-F) cytokine production in Uninf and Uninf+EFZ mono-cultures. IL-8 (C), TNFa (D), IL-1a (E), and IL-1b (F) production in mono-culture did not change for Uninf or Uninf+EFZ. n=4 independent differentiations of WT6, one-way ANOVA, Dunnett's post hoc analysis, error bars represent SEM.

(G) Uninf+ Veh. had minimal but significant increases in IL-8 and IL-1a production at D3, but no increase at D12 where infected cultures had significant increases. n=3 independent differentiations of WT6, one-way ANOVA, Dunnett's post hoc analysis, ***$p<0.001$, error bars represent SEM.

(H&I) No change in tri-culture IL-10 (H) for any of the four conditions, but IL-6 (I) production increased over time for Uninf, and. n=3 independent differentiations of WT6, two-way ANOVA, Tukey's post hoc analysis, **$p<0.01$; ****$p<0.0001$, error bars represent SEM.

A

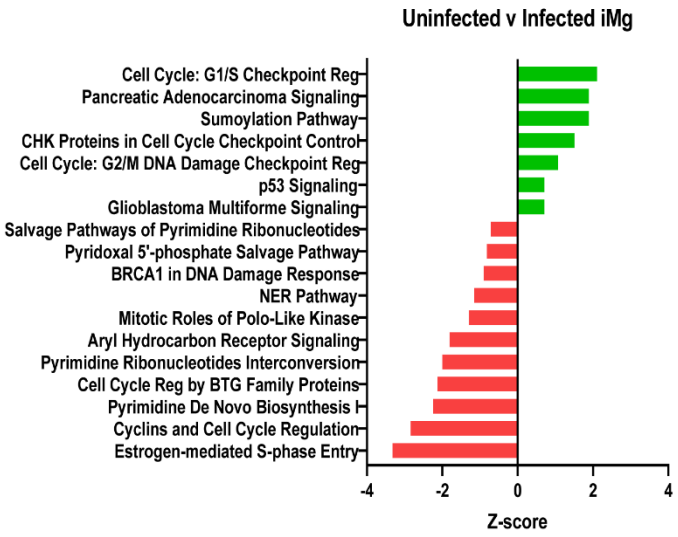

B

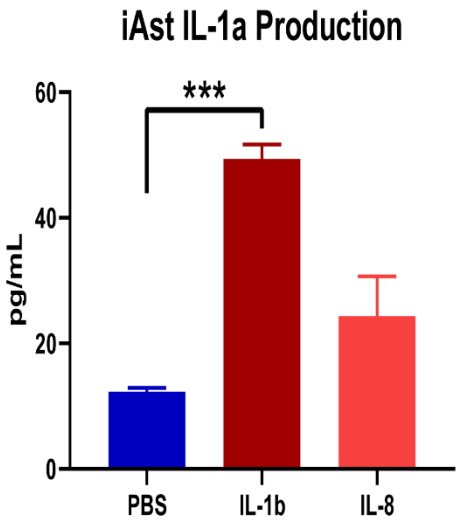

C

Gene	log2fold change	FDR
CCL8	4.425125	0.026731
C5AR1	1.249691	0.026599
C2	1.305198	4.56E-05
CD80	3.148555	3.43E-05
NFKBIZ	1.866165	0.003559
NFKBID	1.53444	0.000622
FOS	2.185966	0.003814
IL1B	2.164145	0.001461
PTGS2	3.682552	0.002386
ATF3	2.755115	9.45E-07
CXCR2	1.056328	0.02422
TNFRSF11A	2.065118	0.009194
TNFRSF10B	1.299788	0.00607

Figure S3: Bulk RNAseq analysis of uninfected versus infected iMg in mono-culture and IL-1a production in iAst. Related to Figures 2 and 3

(A) Ingenuity Pathway Analysis of Uninfected v Infected iMg bulk RNAseq. n=3 cell lines, Fisher's exact <0.05. Benjamini-Hochberg FDR 0.05.

(B) iAst produced IL-1a in response to 8hr exposure to IL-1b (10ng/mL), but not IL-8 (10ng/mL). n=3 cell lines, one-way ANOVA, Dunnett's post hoc analysis, ****p<0.0001, error bars represent SEM.

(C) Select inflammation related genes upregulated in iMg+HIV bulk RNA-seq. Log2fold change at least 1 and FDR <0.05.

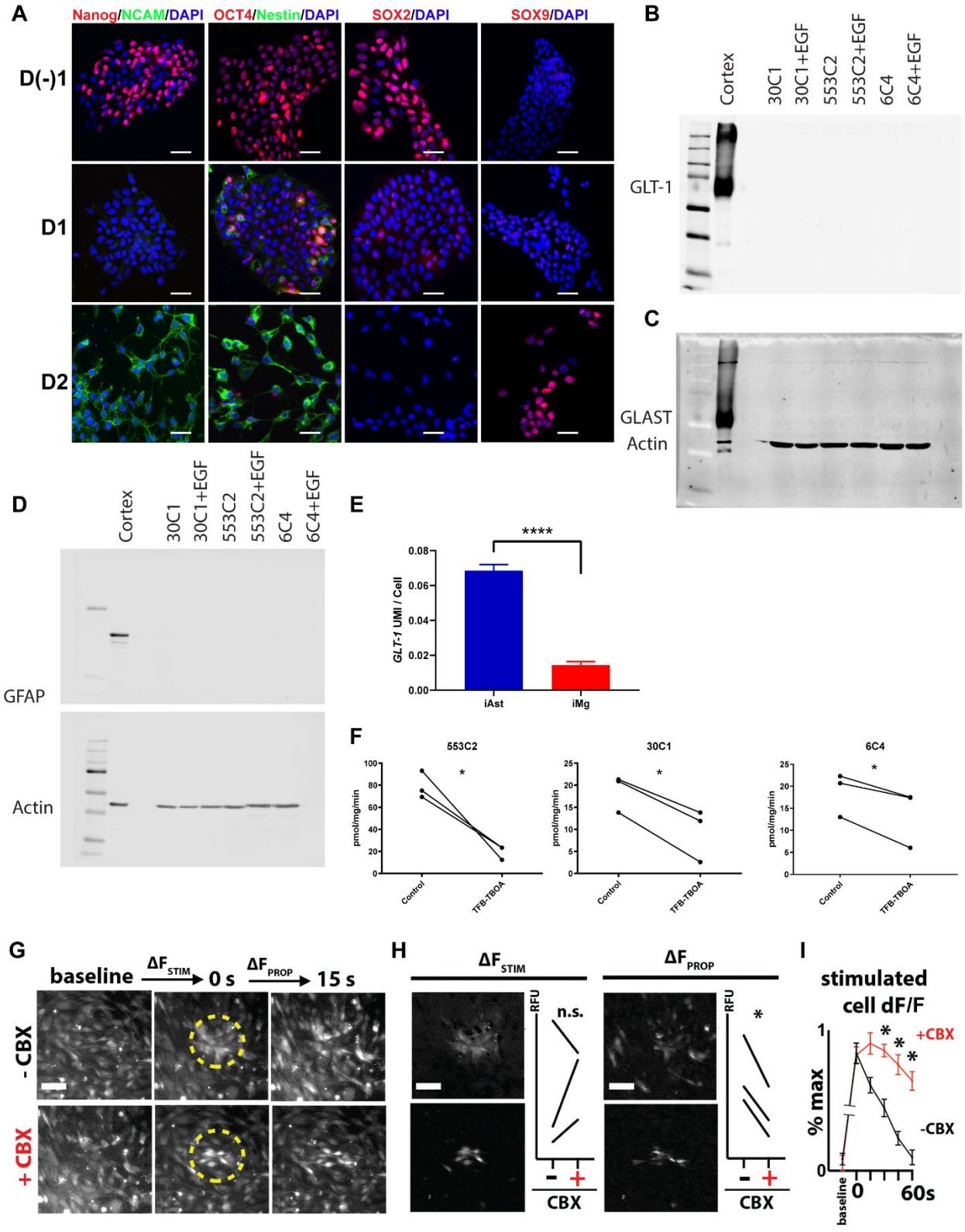

Figure S4: Characterization of iAsts. Related to Figure 3

(A) By day 2 of the NGN2 differentiation (post puromycin selection), cells express have lost pluripotency markers (Nanog, OCT4, and Sox2) and begin to express neural progenitor markers Nestin and NCAM, as well as, the astrocyte marker Sox9. Scale bar represents 25µm.
(B-D) Western blot showing iAst do not express glutamate transporter GLT-1 (B), GLAST (C), or GFAP (D) in mono-culture.
(E) scRNAseq analysis shows that, in tri-culture, iAst express *GLT-1*. iAst n=4,763; iMg n=4,485. two-tailed t test, ****$p<0.0001$, error bars represent SEM.
(F) Glutamate uptake assay showing uptake by three iAst lines and impaired uptake with exposure to glutamate transporter inhibitor TFB-TBOA. n=3 independent experiments for each cell line. Two-tailed paired t test. *$p<0.05$.
(G) Representative images of trans-cellular calcium propagation in iAst mono-culture ± 100µM carbenoxolone (CBX). ΔFstim is the change in fluorescence from baseline to stimulation within the central region. Dotted circle denotes initial stimulation area. ΔFprop is the change in the surrounding region's fluorescence between 0 and 15 seconds. Center region radius = 100µm; Surround region radius = 200 µm. Scale bar represents 50µm.
(H) Representative ΔFstim and ΔFprop images, along with summary graphs that include all three lines. CBX does not significantly influence connexin-independent ΔFstim, while CBX does significantly reduce fluorescence propagation (ΔFprop). RFU=relative fluorescent units. n=3 cell lines (3 technical replicates per line). Two-tailed paired t test. n.s.= not significant, *$p<0.05$.
(I) Change in dF/F of individual cells that were mechanically stimulated. CBX significantly decreases decay rate of dF/F. n=3 cell lines (3 technical replicates per line). Two-way ANOVA, Sidak's post hoc analysis, error bars represent SEM. *$p<0.05$.

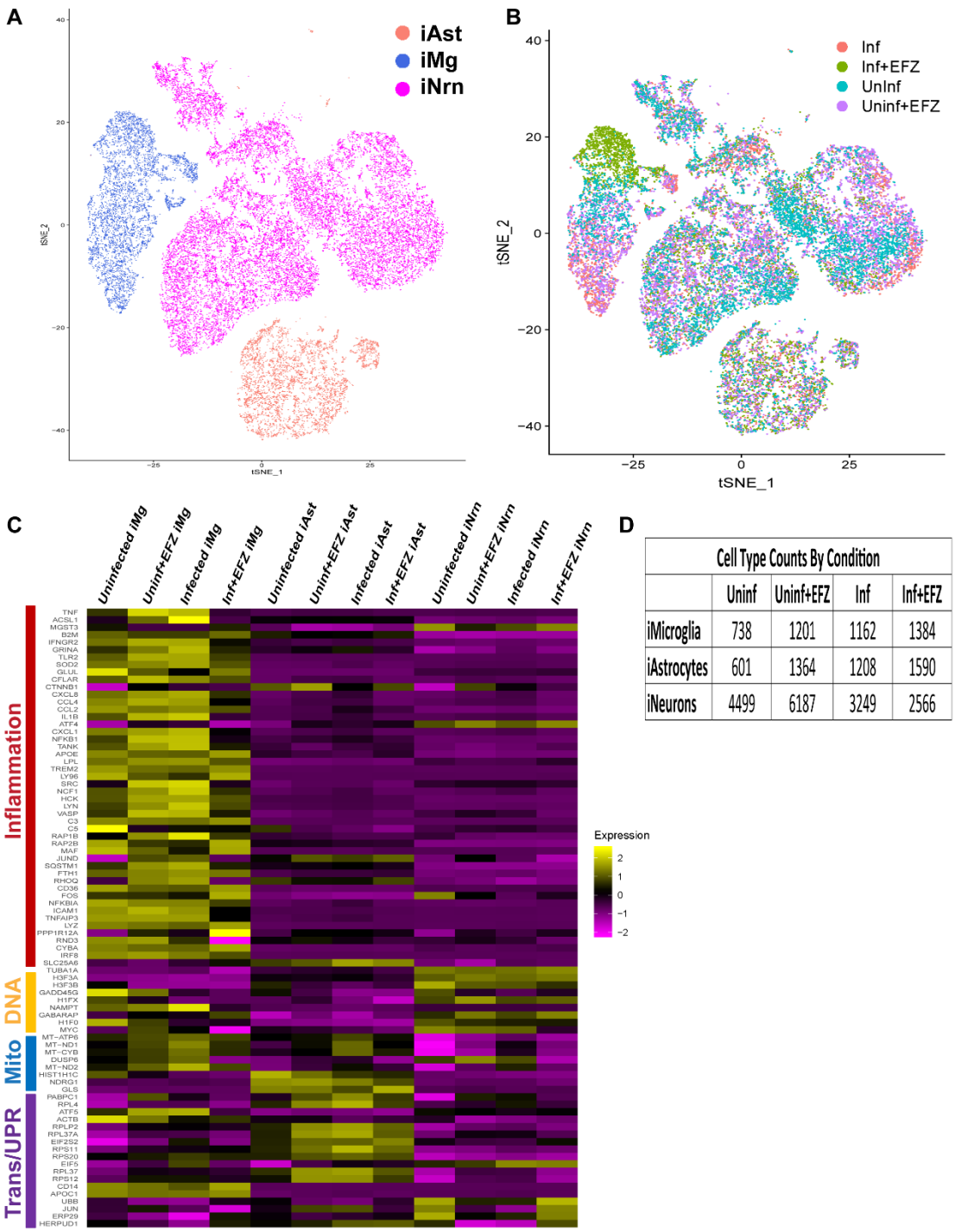

D

Cell Type Counts By Condition				
	Uninf	Uninf+EFZ	Inf	Inf+EFZ
iMicroglia	738	1201	1162	1384
iAstrocytes	601	1364	1208	1590
iNeurons	4499	6187	3249	2566

Figure S5: iMg exhibit the largest inflammatory response by gene expression among the three cell types in tri-culture. Related to Figures 4 and 5

(A) t-SNE plot of all cells from all conditions excluding the undesignated cluster.

(B) t-SNE from (A) broken down by condition.

(C) Heatmap of inflammation, DNA accessibility, mitochondria, and translation/UPR related genes in iAst, iNrn, and iMg in all four conditions: Uninf, Uninf+EFZ, Inf, Inf+EFZ.

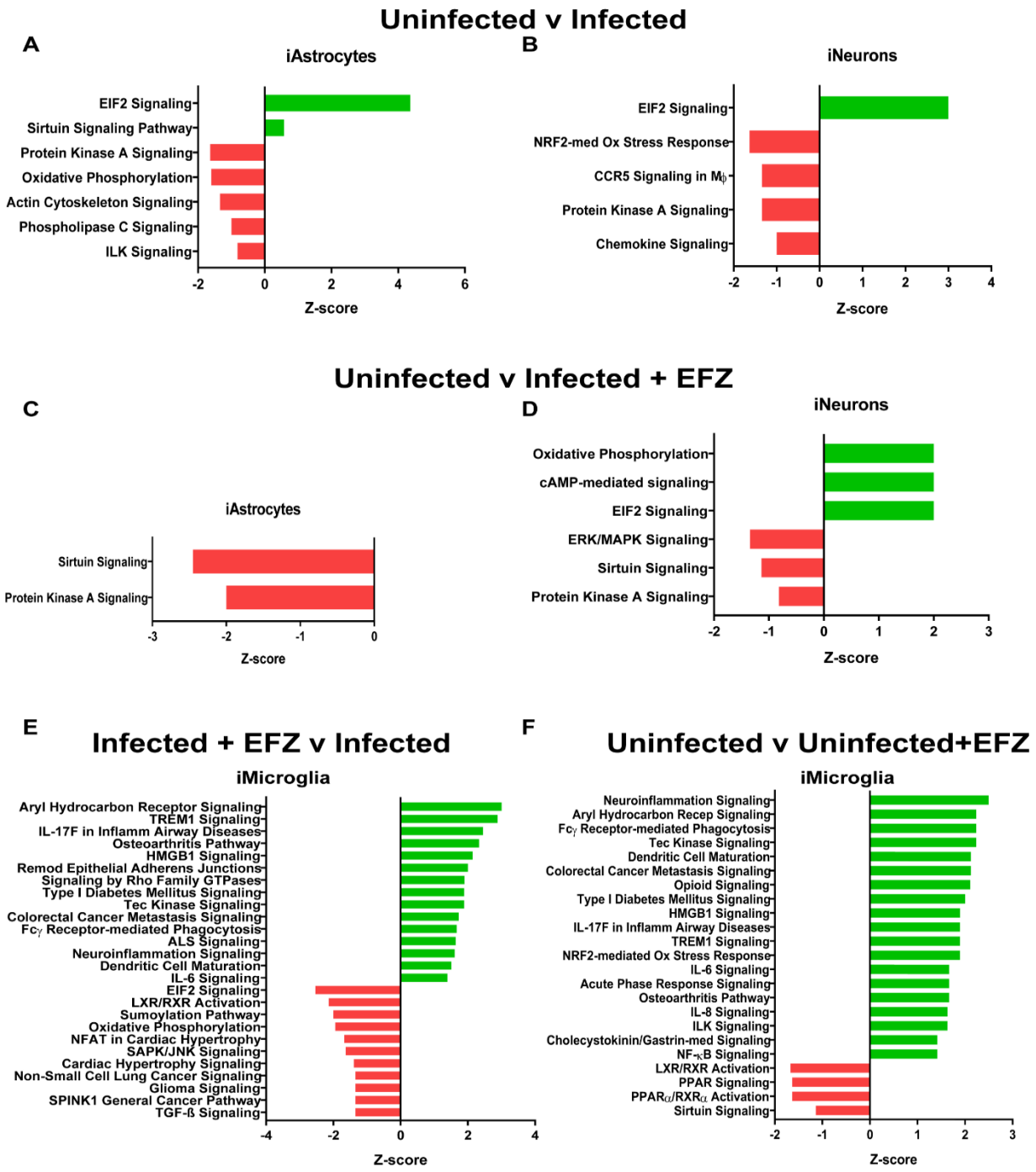

Figure S6: iAst and iNrn Ingenuity pathway analysis for Uninf v Inf, Uninf v Inf+EFZ, and Inf+EFZ v Inf. Related to Figures 5 and 6.

(A&B) Top affected pathways from Ingenuity pathway analysis of iAst (A) and iNrn (B) in the uninfected versus infected conditions. Uninfected is baseline. Benjamini-Hochberg FDR 0.05, Fisher's exact <0.05, z-score cutoff ± 0.5.

(C&D) Top affected pathways from Ingenuity pathway analysis of iAst (C) and iNrn (D) in the uninfected versus infected + EFZ conditions. Uninfected is baseline. Benjamini-Hochberg FDR 0.05, Fisher's exact <0.05, z-score cutoff ± 0.5.

(E&F) Top affected pathways from Ingenuity pathway analysis of Inf+EFZ v Inf iMg (E) and Uninf v Uninf+EFZ iMg (F) Inf+EFZ is baseline in (E) and Uninf is baseline in (F). Benjamini-Hochberg FDR 0.05, Fisher's exact <0.05, z-score cutoff ± 0.5.

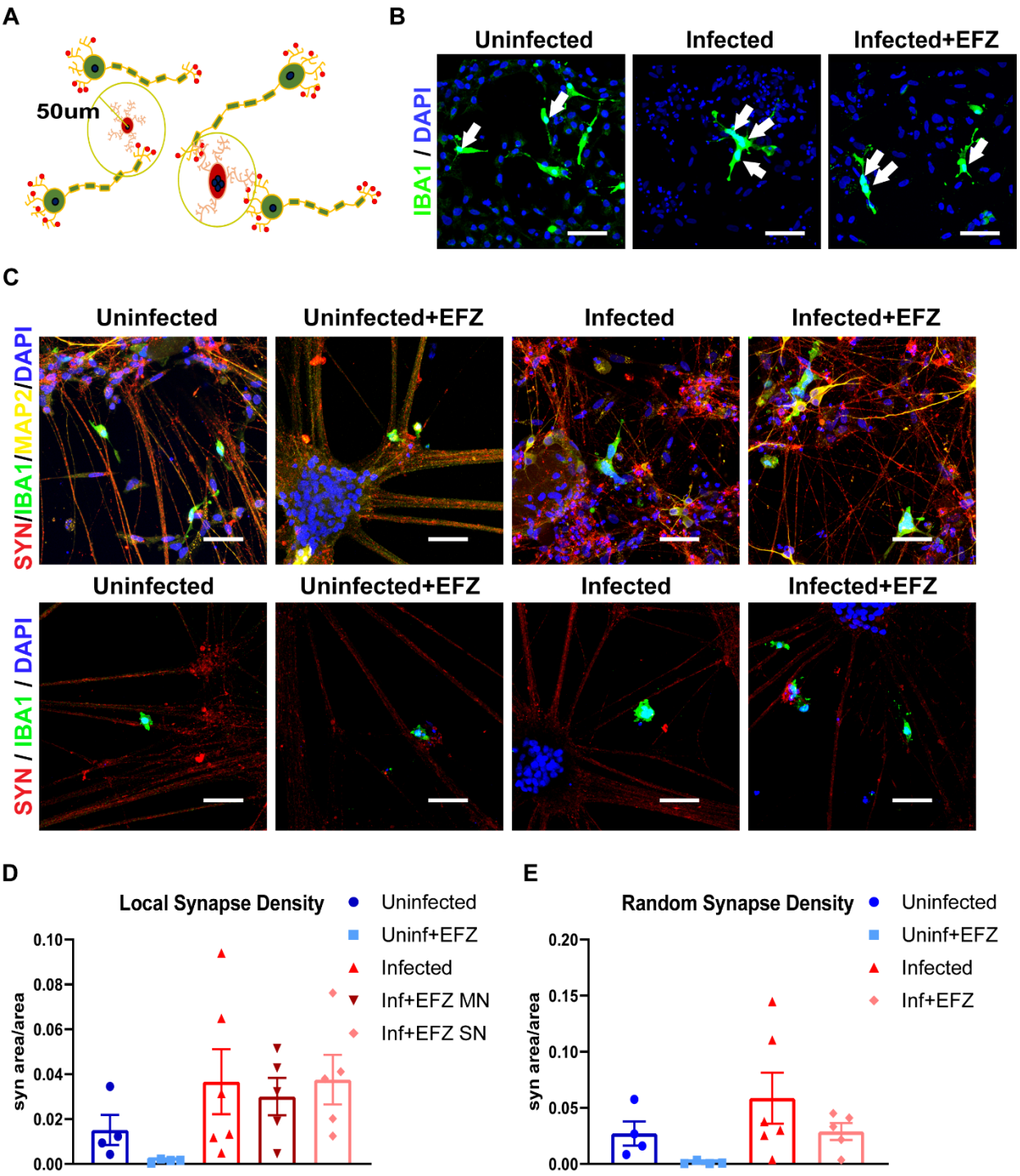

Figure S7: No change in synaptic density local to microglia or throughout the culture. Related to Figure 6.
(A) Cartoon representation of synaptic density analysis
(B) Immunostaining of IBA1+ (green) iMg in Uninf, Inf, and Inf+EFZ tri-cultures depicting multi-nucleated iMg in the infected condition and multi- and single-nucleated iMg in the Inf+EFZ condition. Scale bar represents 50 µm.
(C) Representative images for overall health and analysis of local synapse density measured by density of synaptophysin+ (red) staining within a 50um radius of IBA1+ (green) iMg. MAP2+ neurons (yellow) and DAPI (blue). Scale bar represents 50 µm.

(D) No significant difference in local synapse density across conditions compared to control. n= 4 independent differentiations of WT6 (Uninf=4, Uninf+EFZ=4, Inf=6, Inf+EFZ=5). One-way ANOVA, Dunnett's post hoc analysis, error bars represent SEM.
(E) No significant difference in random synapse density across conditions compared to control. One-way ANOVA, Dunnett's post hoc analysis, error bars represent SEM.

Supplemental Experimental Procedures

Human induced pluripotent stem cell lines

HiPSC lines for the iNrn (6c4) and iAst (6c4, 553c2, and 30c1) were generously received from Herbert M. Lachman, MD., Einstein University, Bronx, New York. All lines were reprogrammed with episomal vectors. All lines trained over to a feeder-free system with Stem MACS iPS-Brew XF media (Miltenyi Biotec 130-104-368). Lines were tested for mycoplasma using Lookout mycoplasma PCR detection kit (Sigma MP0035). iPSC lines for the iMg (CHOPWT4, CHOPWT6, CHOPWT10, CHOPWT15) were cultured by the Human Pluripotent Stem Cell Core (CHOP). All lines were reprogrammed with Sendai viral vectors (Cytotune 2.0, Invitrogen).

Detailed CMP differentiation protocol

As described in (Paluru et al., 2014), differentiation began once iPSCs reached ~70% confluency. All three base media were supplemented with 2 mM glutamine, 50µg/ml ascorbic acid (Sigma), 150µg/ml transferrin (Roche Diagnostics), and 400 µM monothioglycerol (MTG) (Sigma). The base media were RPMI (Invitrogen), StemPro-34 (SP-34) (Invitrogen), and serum free differentiation (SFD) media. The cultures were maintained at 37 °C in an environment of 5% CO2,5%O2, and 90%N2. Days 0–1 RPMI with 5 ng/ml BMP4 and 50 ng/ml VEGF, and 1µM CHiR (Tocris 4423); Day 2 RPMI with 5 ng/ml BMP4, 50 ng/ml VEGF and 20 ng/ml bFGF; Day 3 SP34 with 5 ng/ml BMP4,50 ng/ml VEGF and 20 ng/ml bFGF; Days 4–5SP34 with 15 ng/ml VEGF and 5 ng/ml bFGF; Day 6 SFD with 50 ng/ml VEGF, 100 ng/ml bFGF, 50 ng/ml SCF, and 25 ng/ml Flt3L;Days 7–9 SFD with 50 ng/ml VEGF, 100 ng/ml bFGF, 50 ng/ml SCF, 25 ng/ml Flt3L. Fresh media mixes (2 ml/well) were added each day. By day 6, media was increased to 4 ml/well. From days 7 to 9, single cells shed off the adherent layer into the medium and were collected. CMPs were frozen at 1-3 million cells per vial in 90%FBS and 10% DMSO.

iAstrocyte passaging

After puromycin selection on DIV1 of NGN2 differentiation, NPCs are replated on DIV2 at 100,000 cells/cm^2. Once cells reach 95% confluency, iAstrocytes were washed 2x with PBS and then lifted with StemPro accutase (Thermo Fisher Scientific A11105-01) for 5 min at 37ºC and then spun down at 1,000 rpm for 5 min and split 1:3. Cells were plated to plastic with no additional coating. This was consistent through the entire differentiation.

iAstrocyte cryopreservation

iAstrocytes were washed 2x with PBS and then lifted with StemPro accutase (Thermo Fisher Scientific A11105-01) for 5 min at 37ºC and then spun down at 1,000 rpm for 5 min. Supernatant was aspirated and cell were resuspended in 90% Sciencell Astrocyte Medium and 10% DMSO and frozen at 1 million cells per vial.

HIV infection

iMicroglia were differentiated to D11. On D11, they were exposed to 50ng/mL of JAGO strain HIV (UPenn Center of Aids Research; CFAR) for 24 hours. Media was fully exchange after 24 hours and collected. Full media exchanges occur every 3 days for 15 days. If antiretroviral treatment was used, it was started on day 6 of infection and added with each media exchange. Efavirenz (U.S. Pharmacopeia 1234103) was used at 20nM and Darunavir (Prezista TMC114) at 4.5µM.

RNA extraction

Cells were washed twice with RT PBS, then lifted with StemPro accutase (Thermo Fisher Scientific A11105-01) and spun down at 1,500 rpm for 5 min. Fresh cells were processed through Qiashredder (Qiagen 79654) and RNeasy mini kit (Qiagen 74104) and frozen at -80ºC.

Immunofluorescence

Cells were washed twice with PBS, then fixed in 4% PFA (VWR TCP0018) for 15 min at RT. Cells were washed 3x in PBS for 5 min at RT before being stored in PBS at 4°C. Cells are blocked in 5% BSA (Sigma A9418) and 0.1% Triton X-100 (sigma X100) for 1 hr at RT. Sections use 0.3% Triton-X 100 in blocking buffer. Primary and secondary antibodies were diluted in blocking buffer. Cells were incubated in primary antibodies overnight at 4°C. Cells were washed 3x 5min each at RT in PBS-T (0.1% Tween20) (Sigma P9416). Secondary was performed at RT in the dark for 1 hour. Cells were washed 3x 5min each at RT in PBS-T, then mounted with Prolong gold antifade (Life Technologies P36930).

TMEM119 and DA1E IgG control antibodies required antigen retrieval. Before blocking, cells were heated to 100° C for 4 minutes in 10mM sodium citrate/0.05% tween20, pH 6, then incubated for 15 minutes at RT. After 15 minute incubation, cells were blocked as normal.

Antibodies used for immunofluorescence: Chicken anti-MAP2 (Abcam ab5392, RRID:AB_2138153, 1:500); Mouse anti-PSD-95 clone K28/43 (NeuroMab 75-028, RRID:AB_2292909, 1:500); Mouse anti-Synaptophysin clone SY38 (Millipore MAB5258-20UG, RRID:AB_95185, 1:250); Mouse anti-Nestin clone 10C2 (Millipore MAB5326, RRID:AB_11211837, 1:200); Rabbit anti-Thrombospondin-1 (Abcam ab85762, RRID:AB_10674322, 1:250); Mouse anti-Glutamine Synthetase (Millipore MAB302, RRID:AB_2110656, 1:500); Rabbit anti-SOX9 (Abcam ab185230, RRID:AB_2715497, 1:250); Rabbit anti-CX3CR1 (Abcam ab8021, RRID:AB_306203, 1:500); Rabbit anti-TMEM119 (Abcam ab185333, RRID:AB_2687894, 1:200); Rabbit anti-IBA1 (Wako 019-19741, RRID:AB_839504, 1:500); Rabbit anti-P2RY12 (Alomone Labs APR-020, RRID:AB_11121048, 1:100); Rat anti-LAMP1 (Abcam ab25245, RRID:AB_449893, 1:500); Mouse anti- HIV1 p24 [39/5.4A] (Abcam ab9071, RRID:AB_306981, 1:500); Rabbit anti-Human Nanog (Cell Signaling Technology 3580, RRID:AB_2150399, 1:800); Mouse anti-NCAM Clone 2-2b (Millipore MAB5324, RRID:AB_95211, 1:250); Rabbit anti-OCT-4 (Cell Signaling Technology 2750, RRID:AB_823583, 1:200); Rabbit anti-SOX2 (Millipore AB5603, RRID:AB_2286686, 1:100); Rabbit anti-CCR5 (Thermo Fisher Scientific pa5-29011, RRID:AB_2546487, 1:500); Mouse anti-GLAST (Miltenyi Biotec 130-095-822, RRID:AB_10829302, 1:50); Mouse anti-GFAP (Sigma-Aldrich SAB1405864, RRID:AB_10739114, 1:10,000); Mouse anti-Beta-Actin (Cell Signaling Technology 3700, RRID:AB_2242334, 1:10,000); Rabbit anti-EAAC1 (Santa Cruz Biotechnology sc-25658, RRID:AB_2190727, 1:50); Rabbit GLT-1 (Jeff Rothstein Lab 1:5,000); Rabbit anti-DA1E IgG XP isotype control (Cell Signaling Technology 3900S, RRID: AB_1550038, 1:200); Goat anti-mouse IgG (H+L) Alexa Fluor 488 (Thermo Fisher Scientific A-11029, RRID:AB_138404, 1:500); Goat anti-rabbit IgG (H+L) Alexa Fluor 488 (Thermo Fisher Scientific A-11034, RRID:AB_2576217, 1:500); Goat anti-mouse IgG (H+L) Alexa Fluor 568 (Thermo Fisher Scientific A-11004, RRID:AB_2534072, 1:500); Goat anti-rabbit IgG (H+L) Alexa Fluor 568 (Thermo Fisher Scientific A-11036, RRID:AB_10563566, 1:500); Goat anti-rat IgG (H+L) Alexa Fluor 568 (Molecular Probes A-11077, RRID:AB_141874, 1:500); Goat anti-rat IgG (H+L) Alexa Fluor 680 (Molecular Probes A-21096, RRID:AB_141554, 1:500); Goat anti-Chicken IgY (H+L) DyLight 680 (Thermo Fisher Scientific SA5-10074, RRID:AB_2556654, 1:500)

iAstrocyte/ iMicroglia immunofluorescence counting

Images were obtained with a Nikon eclipse N1 scope equipped with LED-based epifluorescence. The optical fractionator workflow mode of Stereo Investigator 64 bit was then used to generate random areas of the wells to image. 3-5 images were obtained per well. Images were then transferred to image J where the channels were manually merged. After merging images, the "cell count" plugin of imageJ was used to manually quantify the total number of DAPI (+) cells, and the number of co-labeled DAPI+ astrocyte marker(+) or microglia marker (+) cells. Cells were manually counted positive by higher intensity fluorescence over negative secondary control. In the P24 staining experiments, multinucleated cells were counted by the number of DAPI+ nuclei per cell mass, as these were initially multiple cells that became infected and went through syncytia.

Local Synapse Density

Images were analyzed on ImageJ. The iMicroglia were outlined and had a 50μm radius circle drawn from the center of the cell with ROI manager. The total synapse density was measured using the analyze particles plugin. The plugin was used for the ROI of the cell and the surrounding circle. The area of the cell and the area of the particles were subtracted from the total area of the circle and the total particles. The remaining total area of the particles was divided by the remaining total area of the circle to calculate local synapse density.

iAstrocyte Glutamate Uptake

iAst plated in 12-well dishes were placed in a 37°C waterbath and rinsed twice with 1ml of either sodium or choline containing buffer (5mM Tris Base, 10mM HEPES, 2.5mM KCl, 1.2mM CaCl2 2H2O, 1. mM MgCl 6H2O, 1.2mM K2HPO4, 10mM Dextrose and 140mM NaCl or 140 mM choine chloride). The cells were then incubated with 0.5μM [3H]-Glutamate for 5 min in the absence or presence of 3mM TFB-TBOA (Tocris; cat #2532) for 5 minutes. Assays were ceased with the addition of 1 mL 4°C choline-containing buffer then solubilized in 1 mL of 0.1 N sodium hydroxide. An aliquot (500 μl) was combined with 5 ml of EcoLite (MP Biomedicals; cat #SKU 0188247501) and radioactivity was measured using a Beckman scintillation counter. Na+-dependent transport was calculated as the

difference in radioactivity in the presence or absence of sodium and normalized to the amount of protein per well (Lowry protein assay).

Calcium wave propagation assay

iAstrocytes were tested for gap junction-dependent calcium wave propagation similarly to (Fujii, Maekawa, & Morita, 2017). iAstrocytes were grown on Matrigel (Corning 354230) (1:25 DMEM) coated glass coverslips at 90,000cells/cm^2 and grown for one week in Astrocyte media (Sciencell 1801). Cells were washed 2x with RT HBSS (Corning MT21023CV) and then incubated in HBSS with 4µM Fluo-4 AM (Thermo-Fisher Scientific F14201) for 30min at 37° C. Cells were then washed 3x with HBSS and then left in in HBSS for imaging. Cells treated with carbenoxolone, a gap junction blocker, were incubated in HBSS with 100µM carbenoxolone for 10 minutes before imaging. All epifluorescence images were acquired with an exposure of 500ms under 10x magnification using a Nikon eclipse Ti-U microscope. The first baseline image was acquired prior to mechanical stimulation of cells with a 3-5MOhm borosilicate pipette pulled with a Sutter P-97 Micropipette Puller. Pipettes were slowly advanced toward individual cells using a micromanipulator. t=0 images were captured immediately following visual confirmation of cell stimulation. Images were acquired every subsequent 15 seconds for 60 seconds.

Calcium wave analysis

The time-series of six images were combined into a virtual stack of spatially registered images using the ImageJ plugin Turboreg (rigid body translation). Both ΔFsti and ΔFprop were calculated using regional changes in fluorescence. ΔFstim was defined as change in total fluorescence intensity from baseline to t=0sec within the Center/Stimulation Region (within 100um of stimulation point). ΔFprop defined as change in total fluorescence intensity from t=0sec to t=15sec within the Surround Region (the adjacent outer-ring region extending 100um from the Center Region). Because mechanical stimulation of the cells with the micromanipulator increased risk of shifting the imaging plane, ΔFprop for the surrounding region was defined as F(t=15) – F(t=0).

To determine the rate of efflux from the initially stimulated cells, an average dF/F trace was calculated for each replicate trial. The technical replicates were then averaged to produce one dF/F trace per cell line. For each replicate experiment, individual dF/F cell traces (dF/F= (F-F0)/F0 = (F-F(t=0)) / F(t=0)) were calculated and averaged to determine each replicate's average dF/F trace. ROIs for individual cells were determined using ImageJ's magic wand package for semi-automated segmentation of maximum Z-projections for each stack.

Bulk RNA-seq

RNA was extracted using previously described with RNeasy mini kit (Qiagen 74104) and frozen at -80°C. Samples were sent to the Center for Applied Genomics (CAG) for sequencing. In short, the Illumina TruSeq Stranded Total RNA library kit (Illumina RS-122-2201) for RNA-seq was utilized for preparation of the libraries for sequencing. Libraries were produced using liquid handler automation with the PerkinElmer Sciclone instrument. This procedure started with a ribosomal RNA (rRNA) depletion step. The depletion step uses target-specific oligos with specialized rRNA removal beads to remove both cytoplasmic and mitochondrial rRNA from the total RNA. Following this purification, the RNA was fragmented using a brief, high-temperature incubation. The fragmented RNA was then reverse transcribed into first-strand cDNA using reverse transcriptase and random primers. Second strand cDNA was generated using DNA Polymerase which was then used in a standard TruSeq Illumina-adapter based library preparation. Library preparation consisted of four main steps: unique adapter-indexes were ligated to the RNA fragments, AmpureXP bead purification occurred to remove small library fragments, the libraries were enriched and amplified using PCR, and the libraries underwent a final purification using AmpureXP beads. Upon completion, library quality was assessed using an automated electrophoresis instrument, the PerkinElmer Labchip GX Touch, and qPCR using the Kapa Library Quantification Kit and Viia7 real-time PCR instrument. Libraries were diluted to the appropriate sequencer loading concentration and pooled accordingly to allow for the desired sequencing depth. RNA libraries were sequenced in one lane of the Illumina HiSeq2500 sequencer using the High Output v4 chemistry and paired-end sequencing (2x100bp).

Single Cell RNA-seq cell preparation

Cells were incubated in 0.25% Trypsin+EDTA at 37°C for 8 minutes, put through a cell strainer, and spun down in ice-cold PBS at 4°C for 5 min at 1500 RPM. Cells were resuspended in ice-cold DPBS without Mg^{2+} and Ca^{2+}+0.04% BSA. Up to 20,000 cells were sent for sequencing per sample. Samples were sent to CAG for sequencing.

Bulk RNA-seq analysis

RNA-seq reads were demultiplexed using the DRAGEN genome pipeline (Goyal et al., 2017). FASTQ files were aligned to hg19 reference using the STAR (v.2.6.1) (Dobin et al., 2013) aligner with default settings. Generated BAM files were read into the R statistical computing environment. Gene counts were obtained using the GenomicAlignments package. Differential expression analysis was performed using the R/Bioconductor package DESeq2 which uses a negative binomial model (Love, Huber, & Anders, 2014). Analysis was performed using standard parameters with the independent filtering function enabled to filter genes with low mean normalized counts. The Benjamini-Hochberg adjustment was used to estimate the false discovery rate (Padj) and correct for multiple testing. Genes were then analyzed using the Ingenuity IPA software (QIAGEN Inc.). Additional published RNA-seq data was utilized for comparative analysis from project accession SRP092075 (Abud et al., 2017). Datasets were obtained and converted to fastq format using the Sequence Read Archive (SRA) tool provided by NCBI. Fastq-formatted data was analyzed similarly to the bulk RNA-seq samples using the DRAGEN pipeline and integrated into the experimental R data object.

Single Cell RNA-seq analysis

Next-generation sequencing libraries were prepared using the 10x Genomics Chromium Single Cell 3' Reagent kit v2 per manufacturer's instructions. Libraries were uniquely indexed using the Chromium i7 Sample Index Kit, pooled, and sequenced on an Illumina Hiseq sequencer in a paired-end, single indexing run. Sequencing for each library targeted 20,000 mean reads per cell. We had a mean of 39,227 reads per cell post-normalization with 2,165 median genes per cell. Data was then processed using the Cellranger pipeline (10x genomics, v.3.0.2) for demultiplexing and alignment of sequencing reads to the GRCh38 transcriptome and creation of feature-barcode matrices. Individual single cell RNAseq libraries were aggregated using the cellranger aggr pipeline. Libraries were normalized for sequencing depth across all libraries during aggregation. Secondary analysis on the aggregated feature barcode matrix was performed using the Seurat package (v.3.0) within the R computing environment. Briefly, cells expressing less than 200 or more than 5000 genes were excluded from further analysis. Additionally, cells expressing >20% mitochondrial genes were excluded from the dataset. Log normalization and scaling of features in the dataset was performed prior to principal component dimensionality reduction, clustering, and visualization using tSNE. Cell types were identified using expression of canonical cell markers in microglia (AIF1, SPI1, CD4), neurons (MAP2, SYN1), and astrocytes (THBS1, SOX9). Differentially expressed genes and identification of cluster or cell type specific markers were identified using a wilcoxon rank sum test between two groups. P-value adjustment was performed using bonferroni correction based on total number of genes in the aggregated dataset. Genes were then analyzed using the Ingenuity IPA software (QIAGEN Inc.).

qRT-PCR

RNA was extracted by RNeasy mini kit (Qiagen 74104). cDNA was generated using SuperScript VILO Master mix (Thermo Fisher Scientific 11755050). RNA expression was measured using Taqman probes (Thermo Fisher Scientific) for *CX3CR1* (Hs01922583_s1), *P2RY12* (Hs01881698_s1), *TMEM119* (Hs01938722_u1), *THBS1* (Hs00962908_m1), and *GAPDH* (Hs02786624_g1). 30ng of cDNA was used per well, with three technical replicates per probe per sample. qRT-PCR is run on an Applied Biosystems 7900HT Fast Real-Time PCR System. All expression levels were normalized to *GAPDH* expression.

Reverse transcriptase activity

10 µl per well of supernatant was placed into a 96-well microtiter plate to be analyzed for RT activity. 50 µl of RT cocktail was added per well into the 96-well microtiter plate. RT cocktail consists of: 50mM Tris (Amresco J837) pH 7.8, 75mM KCl (Ambion 9610), 2mM Dithiothreitol (DTT) (Sigma D0632), 5mM Magnesium Chloride (Ambion 9530G), 5ug/mL Polyadenylic acid (GE Healthcare 27-4110-01), 2.5ug/mL pd (t)12-18 (Oligo dT) (USB Corporation #19817), 0.05% NP-40 (Calbiochem 492016), 10 µCi/ml Thymidine 5'-triphosphate, ALPHA-[32P] / [32P] TTP (Perkin Elmer BLU005A250MC). Samples were incubated at 37° C overnight. 30 µl of RT reaction mixture was placed onto pre-marked DE81 paper (Whatman 3658915) and air dried for 15 min at RT. Paper was washed 4x, 5 min each with 2x SSC (Roche-Apply science 11 666 681 001) by submerging in a tray on a rotating platform. Paper was then washed 1x, 1 min in 100% ethanol and air dried in an oven at 80-100° C (25-30 min). Each paper sample was placed into a scintillation vial. 5 ml Betaflour (National Diagnostics LS-151) was added to each scintillation vial. 32P was counted on a scintillation counter, yielding CPM.

PCR for CCR5Δ32 mutation

DNA was isolated with DNeasy blood and tissue kit (Qiagen 69504). DNA Oligos were generated by IDT. Forward primer: 5' – CAAAAAGAAGGTCTTCATTACACC – 3'. Reverse primer: 5' –

CCTGTGCCTCTTCTTCTCATTTCG – 3'. Primers were reconstituted to 100uM. Mastermix consists of 10uL KAPA PCR buffer, 7uL H20, 1uL 10uM forward primer, 1uL 10uM reverse primer. 1uL DNA added separately. 1.5% agarose gel was run for 1hour at 120v. The gel was imaged on a Biorad Universal Hood II Gel Doc System.

Western Blot

iAst plated in 12-well dishes were rinsed twice with PBS containing 0.1 mM Ca^{2+} and 1.0 mM Mg^{2+} (PBS Ca^{2+}/Mg^{2+}) then lysed in 200ul of radioimmunoprecipitation (RIPA) buffer for 1 hour while rotating on a shaker at 4ºC. Cortical and hippocampal tissue was harvested from adult C57BL/6 mice and solubilized in 5 volumes of homogenization buffer (50 mM Tris-HCl, pH 7.4, 150 mM NaCl, 5 mM EDTA, 1% NP-40, 1% SDS, containing protease and phosphatase inhibitors, including 1 mg/ml leupeptin, 250 mM phenylmethylsulfonyl fluoride, 1 mg/ml aprotinin, 1 mM iodoacetamide, 10mM NaF, 30mM Na pyrophosphate, 1mM Na^3VO^4). All lysates were centrifuged at 17,000g for 20 min to remove cellular debris and nuclei. The supernatants were analyzed for total protein using the Pierce protein assay kit according to the manufacturer's instructions. Lysates are diluted 1:1 with 2X Laemmli buffer and either boiled at 95ºC for 5 min (GFAP, Actin) or kept at 25ºC for 45 minutes (GLAST, GLT-1, EAAC1). iAst lysates (20ug) or cortical/hippocampal lysates (5ug) were then resolved by SDS PAGE using 10% BioRad minigels and transferred to Immobilon-FL membranes (Millipore Cat# IPFL00010). Membranes were incubated with blocking buffer (1% non-fat dry milk in TBS-T) for 1 hour at 25ºC prior to probing with primary antibodies diluted in blocking buffer overnight at 4ºC: rabbit anti-GLT-1 (C-terminal directed 1:5,000; Rothstein et al 1994), mouse anti-GLAST (Miltenyi Biotec Cat# 130-095-822, 1:50), rabbit anti-EAAC1 (Santa Cruz Cat# SC-25658, 1:50), mouse anti-GFAP (Cell Signaling Cat#3670S, 1:1,000), and mouse anti-Actin (1:10,000 dilution, Cell Signaling, Cat# 3700S). Membranes were washed with blocking buffer 3 times for 10 min at 25ºC. After the washes, membranes were probed with anti-mouse or anti-rabbit fluorescently conjugated secondary antibodies (LI-COR Biosystems, 1:10,000) for 45 minutes at 25ºC. The membranes were washed 3 times for 10 minutes each then visualized using a LI-COR Odyssey.

Synaptophagocytosis analysis

Confocal images of microglia were analyzed in IMARIS software. IBA1 labeling for the microglia was surfaced, as well as synaptophysin staining. Total volume was taken for the microglia and the synaptophysin staining inside the cells. Total synaptophysin volume per cell was then divided by the cell volume defined by IBA1 labeling. At least 5 cells per condition per biological replicate were counted across at least 4 biological replicates. Each biological replicate is an average of the individual cells counted in that replicate. The average per condition is the average of the biological replicates.

Cytokine analysis

Supernatants were tested for 6 analytes (TNFa, IL-6, IL-8, IL-10, IL-1b, IL-1a) on a custom Human magnetic Luminex plate (R&D systems LXSAHM; run by Penn Mental Health AIDS Research Center (PMHARC)). The plate was run by the Penn Mental Health Aids Research Center on a MAGPIX powered by Luminex XMAP technology.

iAstrocyte cytokine exposure

iAstrocytes in mono-culture were exposed to IL-1b (R&D Systems 201-LB-005) or IL-8 (R&D Systems 208-IL-010) at 10ng/mL or PBS vehicle control for 8 hours. Supernatants were collected and sent for cytokine analysis.

Human astrocytes

Three separate donors for human astrocytes were obtained from Sciencell. Cells were plated on PLL-coated plates (Sigma Aldrich P6282) and grown for two weeks in Astrocyte media (Sciencell 1801) and then RNA was extracted.

Monocyte-derived macrophage differentiation

We receive donated buffy coat from New York Blood Center from three donors (D471, D446, D470). Buffy coat was diluted 1:1 with PBS (without Ca^{2+} and Mg^{2+}) (Invitrogen 14190144). 15 mLs of Ficoll (Sigma Aldrich 26878-85-8) was added to 50mL conical tubes. 25mLs of Buffy Coat/PBS was slowly layered onto the Ficoll. Samples were spun at 1200 rpm for 45 minutes with no brake. The peripheral blood mononuclear cell (PBMC) layer was removed and placed into a new 50mL conical tube, and the volume was brought up to 50mL with PBS. The PBMCs are spun at 450Xg for 10 minutes. The supernatant was discarded, and the pellet resuspended in 10mLs of Red Blood Cell Lysis buffer (Sigma Aldrich 11814389001). Cells were shaking at RT for 10 minutes. Volume was brought up to 50mLs in

PBS and spun at 450Xg for 10minutes. The supernatant was discarded, and the pellet was resuspended in DMEM with 10% FBS + Gentamicin (Thermo Fisher Scientific 15750060). The PBMCs were plated on 6-well tissue culture plate for 5 days. On day 5, a full media exchange was performed and added 10ng/mL Human GM-CSF (Gold Biotechnology 1120-03-20). A half media exchange was performed on day 7. At day 10, RNA was collected from macrophages.

RNA seq analysis Statistics

Benjamini-Hochberg procedure was performed on all bulkRNAseq and sing cell RNAseq data, with an FDR cutoff of 0.01 for bulk RNAseq and 0.05 for scRNAseq. Pathway analysis was performed with Ingenuity Pathway Analysis. All pathways had a Fisher's exact below 0.05.

Supplemental References

Abud, E. M., Ramirez, R. N., Martinez, E. S., Healy, L. M., Nguyen, C. H. H. H. H., Newman, S. A., . . . Blurton-Jones, M. (2017). iPSC-Derived Human Microglia-like Cells to Study Neurological Diseases. *Neuron, 94*(2), 278-293.e279-293.e279. doi:10.1016/j.neuron.2017.03.042

Dobin, A., Davis, C. A., Schlesinger, F., Drenkow, J., Zaleski, C., Jha, S., . . . Gingeras, T. R. (2013). STAR: ultrafast universal RNA-seq aligner. *Bioinformatics, 29*(1), 15-21-21. doi:10.1093/bioinformatics/bts635

Fujii, Y., Maekawa, S., & Morita, M. (2017). Astrocyte calcium waves propagate proximally by gap junction and distally by extracellular diffusion of ATP released from volume-regulated anion channels. *Sci Rep, 7*(1), 13115. doi:10.1038/s41598-017-13243-0

Goyal, A., Kwon, H. J., Lee, K., Garg, R., Yun, S. Y., Kim, Y. H., . . . Lee, M. S. (2017). Ultra-Fast Next Generation Human Genome Sequencing Data Processing Using DRAGEN^{TM} Bio-IT Processor for Precision Medicine. *Open Journal of Genetics, 07*(01), 9-19-19. doi:10.4236/ojgen.2017.71002

Love, M. I., Huber, W., & Anders, S. (2014). Moderated estimation of fold change and dispersion for RNA-seq data with DESeq2. *Genome Biology, 15*(12), 550. doi:10.1186/s13059-014-0550-8

Paluru, P., Hudock, K. M., Cheng, X., Mills, J. A., Ying, L., Galvão, A. M., . . . Gadue, P. (2014). The negative impact of Wnt signaling on megakaryocyte and primitive erythroid progenitors derived from human embryonic stem cells. *Stem Cell Research, 12*(2), 441-451-451. doi:10.1016/j.scr.2013.12.003